

The *R*-Process Alliance: 2MASS J22132050–5137385, the Star with the Highest-known *r*-process Enhancement at $[\text{Eu}/\text{Fe}] = +2.45^*$

IAN U. ROEDERER,^{1,2} TIMOTHY C. BEERS,^{3,2} KOHEI HATTORI,^{4,5} VINICIUS M. PLACCO,⁶ TERESE T. HANSEN,⁷
RANA EZZEDDINE,^{8,2} ANNA FREBEL,^{9,2} ERIKA M. HOLMBECK,^{10,2} AND CHARLI M. SAKARI¹¹

¹*Department of Physics, North Carolina State University, Raleigh, NC 27695, USA*

²*Joint Institute for Nuclear Astrophysics – Center for the Evolution of the Elements (JINA-CEE), USA*

³*Department of Physics and Astronomy, University of Notre Dame, Notre Dame, IN 46556, USA*

⁴*National Astronomical Observatory of Japan, 2-21-1 Osawa, Mitaka, Tokyo 181-8588, Japan*

⁵*The Institute of Statistical Mathematics, 10-3 Midoricho, Tachikawa, Tokyo 190-8562, Japan*

⁶*NSF's NOIRLab, Tucson, AZ 85719, USA*

⁷*Department of Astronomy, Stockholm University, SE-106 91 Stockholm, Sweden*

⁸*Department of Astronomy, University of Florida, Bryant Space Science Center, Gainesville, FL 32611, USA*

⁹*Department of Physics and Kavli Institute for Astrophysics and Space Research, Massachusetts Institute of Technology, Cambridge, MA 02139, USA*

¹⁰*Carnegie Observatories, Pasadena, CA 91101, USA*

¹¹*Department of Physics and Astronomy, San Francisco State University, San Francisco, CA 94132, USA*

(Accepted for publication in the *Astrophysical Journal*)

ABSTRACT

We present stellar parameters and chemical abundances of 47 elements detected in the bright ($V = 11.63$) very metal-poor ($[\text{Fe}/\text{H}] = -2.20 \pm 0.12$) star 2MASS J22132050–5137385. We observed this star using the Magellan Inamori Kyocera Echelle spectrograph as part of ongoing work by the *R*-Process Alliance. The spectrum of 2MASS J22132050–5137385 exhibits unusually strong lines of elements heavier than the iron group, and our analysis reveals that these elements were produced by rapid neutron-capture (*r*-process) nucleosynthesis. We derive a europium enhancement, $[\text{Eu}/\text{Fe}] = +2.45 \pm 0.08$, that is higher than any other *r*-process-enhanced star known at present. This star is only the eighth *r*-process-enhanced star where both thorium and uranium are detected, and we calculate the age of the *r*-process material, 13.6 ± 2.6 Gyr, from the radioactive decay of these isotopes. This star contains relatively large enhancements of elements that may be produced as transuranic fission fragments, and we propose a new method using this characteristic to assess the *r*-process yields and gas dilution in samples of *r*-process-enhanced stars. We conclude that 2MASS J22132050–5137385 exhibits a high level of *r*-process enhancement because it formed in an environment where the *r*-process material was less diluted than average. Assuming a canonical baryonic minihalo mass of $10^6 M_{\odot}$ and a 1% metal retention rate, this star formed in a cloud of only $\sim 600 M_{\odot}$.

Keywords: Nucleosynthesis (1131); *R*-process (1324); Stellar abundances (1577)

1. INTRODUCTION

Understanding the origins of elements across the periodic table remains a major challenge of modern astrophysics. Heavy elements produced by the rapid neutron-capture process, or *r*-process (Cowan et al. 2021), are not distributed evenly throughout the Milky Way and Local Group of galaxies. The enhancement of *r*-process mate-

rial relative to the stellar metallicity is often quantified through the $[\text{Eu}/\text{Fe}]$ ratio¹³. Among the Sun and other metal-rich stars in the Milky Way thin disk, there is a small range in $[\text{Eu}/\text{Fe}]$ of about 0.3–0.4 dex (a factor of 2.0–2.5; e.g., Battistini & Bensby 2016; Delgado Mena et al. 2017; Guiglion et al. 2018). In contrast, metal-poor stars exhibit a large range in $[\text{Eu}/\text{Fe}]$ that varies

Email: iuroederer@ncsu.edu

* This paper includes data gathered with the 6.5 meter Magellan Telescopes located at Las Campanas Observatory, Chile.

¹³ The ratio of the abundances of elements europium (Eu, $Z = 63$) and iron (Fe, $Z = 26$) relative to the Solar ratio, $[\text{Eu}/\text{Fe}]$, is defined as $\log_{10}(N_{\text{Eu}}/N_{\text{Fe}}) - \log_{10}(N_{\text{Eu}}/N_{\text{Fe}})_{\odot}$. We adopt analogous notation for other abundance ratios.

by 3–4 orders of magnitude (a factor of 1,000–10,000) across the Milky Way halo and its dwarf galaxies (e.g., McWilliam 1998; Ji et al. 2020; Li et al. 2022).

Stars with the highest levels of r -process enhancement, defined empirically as exhibiting [Eu/Fe] ratios $> +0.7$ (Holmbeck et al. 2020), are frequently referred to as r -II stars. More than 200 such stars have been confirmed in the Milky Way over the last 30 years, to the best of our knowledge of the literature. The star with the highest known level of r -process enhancement, 2MASS J15213995–3538094 (hereafter J1521–3538), with [Eu/Fe] = $+2.23 \pm 0.12$, was studied in detail by Cain et al. (2020). That study proposed a new class, r -III, to designate r -process-enhanced stars with [Eu/Fe] $> +2$.

2MASS J15213995–3538094 shares the extreme tail of the distribution ([Eu/Fe] $> +1.7$) with five other r -process-enhanced stars known in the Milky Way (Frebel et al. 2007; Aoki et al. 2010; Jacobson et al. 2015; Ezzeddine et al. 2020; Hansen et al. 2021) and several stars in the Reticulum II dwarf galaxy (Ji et al. 2016b, 2023; Roederer et al. 2016; Hayes et al. 2023). Similarly, the Fornax dwarf galaxy contains several metal-poor stars that are extremely enriched in r -process material, [Eu/H] $> +0.0$ (enhanced to [Eu/Fe] $\gtrsim +1.3$ with [Fe/H] $\gtrsim -1.3$; Reichert et al. 2021). All of these stars are members of dwarf galaxies, kinematic substructures associated with disrupted dwarf galaxies (Roederer et al. 2018a; Yuan et al. 2020; Gudín et al. 2021; Hattori et al. 2023; Shank et al. 2023), or stellar streams (Hansen et al. 2021). Many theoretical investigations exploring r -process enrichment in dwarf galaxies indicate that low-rate and high-yield r -process sites can generate extreme r -process enhancements in stars (e.g., Beniamini et al. 2016; Ojima et al. 2018; Molero et al. 2021; Hirai et al. 2022; Cavallo et al. 2023).

The R -Process Alliance (RPA) has been conducting high-resolution spectroscopic observations of metal-poor stars to identify and characterize several hundred new r -process-enhanced stars (Hansen et al. 2018; Sakari et al. 2018; Ezzeddine et al. 2020; Holmbeck et al. 2020). This manuscript details our discovery, analysis, and interpretation of the nature of one extreme r -process-enhanced star. We observed the star 2MASS J22132050–5137385 (hereafter J2213–5137) as part of the RPA activities (Section 2). We recognized the peculiar nature of this star’s optical spectrum, which exhibits hundreds of unusually strong lines of singly ionized lanthanide elements (Section 2.3). Our analysis (Section 3) reveals that this star exhibits the highest level of r -process enhancement known to date (Section 4). We also detect the radioactive actinide elements thorium and uranium in its spectrum (Section 5.2), marking only the eighth time that both elements have been detected together in an r -process-enhanced star. We discuss the kinematics of this extreme star and the circumstances that may have led to its formation (Sec-

tions 5.5 and 5.6). Finally, we summarize our conclusions about the uncommon nature of this star (Section 6).

2. DATA

2.1. Observations

Table 1 lists the basic data for J2213–5137. J2213–5137 was identified as a metal-poor star in the fourth data release (DR4) from the RAdial Velocity Experiment (RAVE; Kordopatis et al. 2013). The RAVE DR4 stellar parameter pipeline returned effective temperature (T_{eff}) of 5870 ± 158 K, log of the surface gravity ($\log g$) of 3.27 ± 0.45 in cgs units, and metallicity ([Fe/H]) of -1.63 ± 0.12 for J2213–5137. This star was not included in the initial set of medium-resolution spectroscopic followup of RAVE targets conducted by the RPA (Placco et al. 2018). Nevertheless, that analysis revealed that the published RAVE stellar parameter estimates were sufficiently reliable to bypass collecting medium-resolution spectroscopic followup for most stars and proceed directly to high-resolution spectroscopic followup.

We observed J2213–5137 on 2021 December 05 with two short (300 s and 500 s) integrations using the Magellan Inamori Kyocera Echelle (MIKE; Bernstein et al. 2003) spectrograph on the Landon Clay (Magellan II) 6.5 m Telescope at Las Campanas Observatory, Chile. This spectrum was obtained using the $0''.7$ slit, resulting in a spectral resolving power of $R \equiv \lambda/\Delta\lambda = 41,000$ at wavelengths < 5000 Å and $R = 35,000$ at wavelengths > 5000 Å. The high signal-to-noise (S/N) ratio of this spectrum, ≈ 80 at 3950 Å, enabled us to immediately recognize the unprecedented situation, shown in Figure 1, wherein the Eu II line at 3819.67 Å appeared stronger than the Fe I line at 3820.42 Å. Unfortunately, poor weather prevented us from obtaining additional followup during this observing run.

We reobserved J2213–5137 with MIKE on 2022 July 22 (4.61 hr) and 2022 August 18 (4.33 hr). Both sets of observations were made with the $0''.35$ slit, binned 1×1 , yielding $R = 60,000$ in the blue and $R = 56,000$ in the red. We used a non-standard blue grating setting to observe orders 109 to 75 (3260–4780 Å) on both nights. On the first night, we also used a non-standard red grating setting to observe orders 72 to 48 (4750–7250 Å). On the second night we used the standard red grating setting to observe orders 70 to 36 (4870–9650 Å). The orders redward of ≈ 8000 Å are marked by fringing, which we have not attempted to correct. We used the CarPy MIKE reduction pipeline (Kelson et al. 2000; Kelson 2003) to perform standard data reduction steps, including overscan subtraction, pixel-to-pixel flat field division, image coaddition, cosmic-ray removal, sky and scattered light subtraction, rectification of the tilted slit profiles, spectrum extraction, and wavelength calibration based on ThAr lamp spectra collected immediately before or after our science exposures. We perform the spectrum

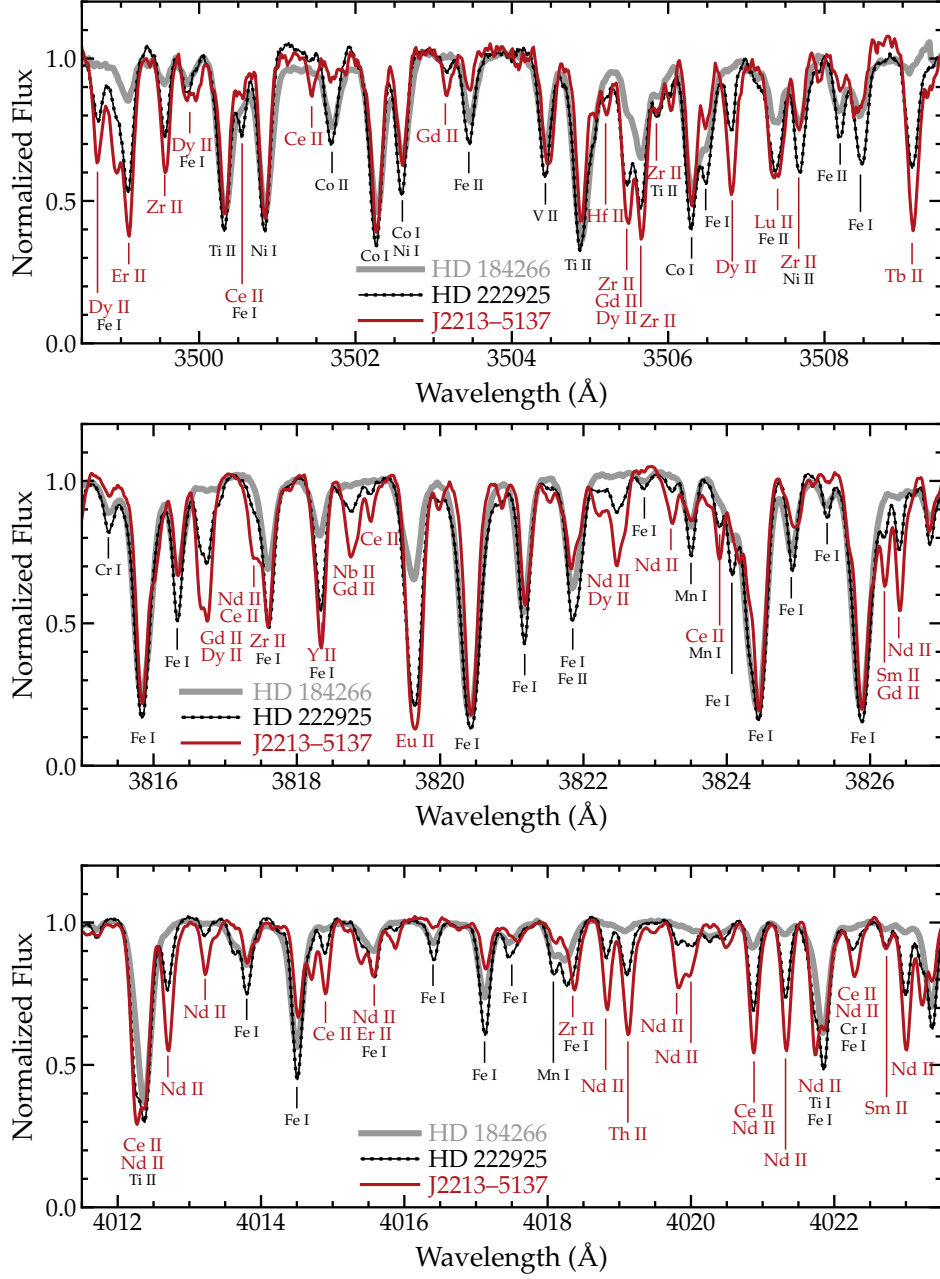


Figure 1. Comparison of the spectra of three stars with similar T_{eff} but contrasting levels of r -process enhancement. HD 184266 has $T_{\text{eff}} = 5580 \pm 102$ K, $[\text{Fe}/\text{H}] = -1.80 \pm 0.08$, and $[\text{Eu}/\text{Fe}] = +0.29 \pm 0.16$ (Roederer et al. 2014, 2018b). HD 222925 has $T_{\text{eff}} = 5636 \pm 103$ K, $[\text{Fe}/\text{H}] = -1.46 \pm 0.10$, and $[\text{Eu}/\text{Fe}] = +1.32 \pm 0.08$ (Roederer et al. 2018b, 2022a). J2213-5137 has $T_{\text{eff}} = 5509 \pm 72$ K, $[\text{Fe}/\text{H}] = -2.20 \pm 0.07$, and $[\text{Eu}/\text{Fe}] = +2.45 \pm 0.08$. Lines of lighter elements are marked in black font, and lines of r -process elements are marked in red font.

Table 1. Properties of J2213–5137

Quantity	Symbol	Value	Units	Reference
Astrometric Properties				
Right ascension	α (J2000)	22:13:20.49	hh:mm:ss.ss	Gaia DR3 (Lindgren et al. 2021)
Declination	δ (J2000)	−51:37:38.7	dd:mm:ss.s	Gaia DR3 (Lindgren et al. 2021)
Galactic longitude	ℓ	342.4	degrees	Gaia DR3 (Lindgren et al. 2021)
Galactic latitude	b	−51.6	degrees	Gaia DR3 (Lindgren et al. 2021)
Proper motion (α)	$\mu_{\alpha*}$	7.012 ± 0.017	mas yr ^{−1}	Gaia DR3 (Lindgren et al. 2021)
Proper motion (δ)	μ_{δ}	−17.524 ± 0.019	mas yr ^{−1}	Gaia DR3 (Lindgren et al. 2021)
Parallax	ϖ	0.4647 ± 0.0186	mas	Gaia DR3 (Lindgren et al. 2021)
Distance	D	2.01 ^{+0.08} _{−0.10}	kpc	Bailer-Jones et al. (2021)
Galactocentric coordinates (Cartesian)	(x, y, z)	(−6.99 ^{+0.05} _{−0.04} , −0.38 ^{+0.01} _{−0.01} , −1.58 ^{+0.06} _{−0.06})	kpc	this study
Galactocentric distance	R	7.00 ^{+0.04} _{−0.05}	kpc	this study
Kinematic Properties				
Radial velocity	v_r	120.59 ± 1.36	km s ^{−1}	RAVE DR5 (Kunder et al. 2017) ^a
Radial velocity	v_r	119.12 ± 0.47	km s ^{−1}	Gaia DR3 (Katz et al. 2022)
Radial velocity	v_r	117.5 ± 0.3	km s ^{−1}	this study ^b
Galactocentric velocity (Cartesian)	(v_x, v_y, v_z)	(32.1 ^{+1.8} _{−1.9} , 52.1 ^{+6.2} _{−6.7} , −80.1 ^{+0.3} _{−0.3})	km s ^{−1}	this study
Galactocentric velocity (cylindrical)	(v_R, v_z, v_{ϕ})	(−34.9 ^{+2.2} _{−2.0} , −80.1 ^{+0.3} _{−0.3} , 50.3 ^{+6.2} _{−6.7})	km s ^{−1}	this study
Integrals of motion	(J_r, J_z, J_{ϕ})	(332.9 ^{+18.5} _{−16.8} , 174.2 ^{+4.2} _{−4.1} , 352.0 ^{+45.8} _{−48.8})	kpc km s ^{−1}	this study
Orbital pericenter	r_{peri}	1.12 ^{+0.15} _{−0.15}	kpc	this study
Orbital apocenter	r_{apo}	7.20 ^{+0.04} _{−0.04}	kpc	this study
Maximum orbital distance from Galactic midplane	$ z_{\text{max}} $	4.04 ^{+0.14} _{−0.13}	kpc	this study
Orbital eccentricity	e	0.73 ^{+0.03} _{−0.03}	...	this study
Photometric Properties				
<i>NUV</i> magnitude	<i>NUV</i>	15.748 ± 0.012	mag	GALEX (Bianchi et al. 2017)
<i>B</i> magnitude	<i>B</i>	12.223 ± 0.008	mag	APASS (Munari et al. 2014)
<i>V</i> magnitude	<i>V</i>	11.630 ± 0.02	mag	APASS (Munari et al. 2014)
<i>G</i> magnitude	<i>G</i>	11.446 ± 0.003	mag	Gaia DR3 (Riello et al. 2021)
<i>BP</i> magnitude	<i>G_{BP}</i>	11.788 ± 0.003	mag	Gaia DR3 (Riello et al. 2021)
<i>RP</i> magnitude	<i>G_{RP}</i>	10.928 ± 0.004	mag	Gaia DR3 (Riello et al. 2021)
<i>J</i> magnitude	<i>J</i>	10.311 ± 0.026	mag	2MASS (Cutri et al. 2003)
<i>H</i> magnitude	<i>H</i>	9.949 ± 0.025	mag	2MASS (Cutri et al. 2003)
<i>K_s</i> magnitude	<i>K_s</i>	9.863 ± 0.023	mag	2MASS (Cutri et al. 2003)
Color excess	$E(B - V)$	0.017 ± 0.01	mag	Schlafly & Finkbeiner (2011)
Bolometric correction	BC_V	−0.31 ± 0.04	mag	Casagrande & Vandenberg (2014)
Model Atmosphere				
Effective temperature	T_{eff}	5509 ± 43 (stat.) ± 72 (sys.)	K	this study
Log of surface gravity	log g	2.28 ± 0.06	(cgs)	this study
Microturbulent velocity	v_t	2.25 ± 0.10	km s ^{−1}	this study
Metallicity	[Fe/H]	−2.20 ± 0.12	...	this study

^a 2009/08/20^b Calculated from three separate MIKE observations: RV = 117.5 ± 0.7 km s^{−1} on 2021/12/05 at UT = 00:33; RV = 117.8 ± 0.7 km s^{−1} on 2022/07/22 at UT = 05:45; and RV = 117.3 ± 0.7 km s^{−1} on 2022/08/18 at UT = 04:25.

coaddition, order stitching, and continuum normalization using routines in the Image Reduction and Analysis Facility (IRAF) “echelle” package (Tody 1993). The S/N per pixel in the coadded spectrum ranges from 70 at 3500 Å, 190 at 3950 Å, 290 at 4550 Å, to >300 at wavelengths longer than 5000 Å.

2.2. Radial Velocity

We compute the radial velocity, v_r , of each of the three observations of J2213–5137 using the echelle order containing the Mg I *b* triplet (≈ 5150 – 5250 Å). We use the IRAF “fxcor” task to cross-correlate this order against a metal-poor stellar template observed using MIKE and shifted to rest velocity (Roederer et al. 2014). The individual v_r measurements are listed in a footnote to Table 1. All agree to within their mutual uncertainties, and no variations are evident from the three observations spanning 8.5 mo. Their mean velocity is 3.1 km s^{-1} different from the v_r measured by RAVE and 1.6 km s^{-1} different from the v_r presented in Gaia’s third data release (DR3; Katz et al. 2022). We observed one radial-velocity standard star on each night using the same MIKE setup, and the v_r for each of those stars agrees with the corresponding Gaia velocity to within $\approx 0.3 \text{ km s}^{-1}$. These measurements could signal that J2213–5137 is in a binary or multiple star system, and we intend to perform periodic radial velocity monitoring of J2213–5137.

2.3. The Rich Spectrum of J2213–5137

Figure 1 shows three regions of the spectrum of J2213–5137 that include numerous lines of heavy elements. Two other stars with similar T_{eff} and $\log g$ values are shown for comparison. HD 184266 is only mildly enhanced in r -process elements ($[\text{Eu}/\text{Fe}] = +0.29 \pm 0.16$; Roederer et al. 2014), while HD 222925 is highly enhanced in r -process elements ($[\text{Eu}/\text{Fe}] = +1.32 \pm 0.08$; Roederer et al. 2022a). J2213–5137 is more metal-poor ($[\text{Fe}/\text{H}] = -2.20 \pm 0.07$; Section 3.1) than either HD 184266 ($[\text{Fe}/\text{H}] = -1.80 \pm 0.08$) or HD 222925 ($[\text{Fe}/\text{H}] = -1.46 \pm 0.10$). This fact is demonstrated in Figure 1 by the relative strengths of lines of iron-group elements. In contrast, the lines of r -process elements are substantially stronger in the spectrum of J2213–5137 than in the spectrum of either comparison star.

As we will show in Section 4, J2213–5137 exhibits an r -process enhancement ($[\text{Eu}/\text{Fe}]$) that is about 13 times higher than HD 222925 and about 280 times higher than the Sun. Similarly, J2213–5137 exhibits an r -process enrichment ($[\text{Eu}/\text{H}]$) that is about 2.4 times higher than HD 222925 and about 1.8 times higher than the Sun. In other words, per unit mass there are nearly twice as many atoms of r -process elements in J2213–5137 than in the Sun, despite the overall factor of 160 difference in metallicity. This contrast is evident among the lanthanide and actinide elements, which exhibit numerous strong lines in the spectral regions shown in Figure 1.

The spectrum of J2213–5137 presents a remarkable opportunity to study the r -process abundance pattern.

3. ANALYSIS

3.1. Model Atmosphere Parameters

We measure equivalent widths (EWs) of Fe I and II lines using a semi-automated routine that fits line profiles in continuum-normalized spectra (Roederer et al. 2014). This routine uses an iterative clipping procedure to identify the local continuum of an ≈ 7 Å region around the line of interest, which can subsequently be modified by the user if necessary. It then fits a Voigt profile, which defaults to a Gaussian profile for the vast majority of lines, to the line of interest, and it integrates the EW under this fit.

Table 2 lists the line wavelengths (λ), excitation potential (E.P.) of the lower level, $\log(gf)$ values, and references for the $\log(gf)$ values. Table 2 also lists any hyperfine splitting (HFS) and isotope shifts (IS) used to compute the line component patterns, equivalent widths (EW), abundances computed assuming local thermodynamic equilibrium (LTE), upper limit (U.L.) flags, and non-LTE (NLTE) corrections. The abundances derived from these lines, along with broadband photometry and astrometry from the Gaia mission (Gaia Collaboration et al. 2016, 2022) and other public resources, help determine the model atmosphere parameters.

We use the LTE line analysis code MOOG (Snedden 1973; Sobek et al. 2011) to derive abundances from these EWs and a model atmosphere. We interpolate a model atmosphere from the α -enhanced grid of one-dimensional ATLAS9 models (Castelli & Kurucz 2004) using a code provided by A. McWilliam (2009, private communication).

We calculate the effective temperature, T_{eff} , using the color-metallicity- T_{eff} calibrations provided by Mucciarelli et al. (2021) for Gaia and 2MASS broadband photometry. We adopt an initial metallicity estimate of $[\text{Fe}/\text{H}] = -2.0$. Six color combinations are constructed among the Gaia G , G_{BP} , G_{RP} , and 2MASS K_s magnitudes. We deredden these colors using the $E(B - V)$ color excess inferred from the dust maps of Schlafly & Finkbeiner (2011) and the extinction coefficients presented by Gaia Collaboration et al. (2018). The amount of interstellar absorption at the stronger component of the Na I *D* doublet does not exceed 45 mÅ . This translates (Roederer et al. 2018c) to a low $E(B - V)$, $< 0.01 \text{ mag}$ or so, supporting the low extinction value inferred from the dust maps (Table 1).

We estimate the statistical uncertainty in T_{eff} by resampling each of these input parameters and recalculating T_{eff} 10^4 times. Each parameter is resampled from a Gaussian distribution with a mean equal to the parameter’s value and a standard deviation equal to the parameter’s 1σ uncertainty. We calculate the weighted mean of the six predicted T_{eff} values, 5509 K , and we adopt it as the final T_{eff} for J2213–5137. We estimate the

systematic uncertainty in T_{eff} by performing analogous calculations using the color-metallicity- T_{eff} calibrations presented by [Alonso et al. \(1999\)](#), [Ramírez & Meléndez \(2005\)](#), and [Casagrande et al. \(2010\)](#). These studies calibrated several sets of colors among B and V Johnson photometry and J , H , and K_s (or K_{TCS}) photometry. These alternative scales predict $T_{\text{eff}} = 5467 \pm 108$ K, 5417 ± 58 K, and 5612 ± 67 K, respectively. We adopt the standard deviation of these four values as an approximate lower limit on the systematic uncertainty in T_{eff} . Table 1 lists our adopted T_{eff} value for J2213–5137, 5509 ± 43 (stat.) ± 72 (sys.) K.

We calculate the log of the surface gravity, $\log g$, using the fundamental relations expressed in equation 1 of [Roederer et al. \(2018b\)](#). The relevant quantities for J2213–5137 are listed in Table 1, and we assume a mass of $0.80 \pm 0.08 M_{\odot}$. We resample each of the input parameters 10^4 times. We adopt the median value of this distribution as $\log g$, and we adopt the standard deviation of these values as its uncertainty: 2.28 ± 0.06 . The T_{eff} and $\log g$ of J2213–5137 imply that it is a field-star equivalent of the red horizontal branch found in globular clusters.

We interpolate a model atmosphere for these T_{eff} and $\log g$ values, and we use MOOG to derive the abundance from each Fe I and II line. We adopt the microturbulent velocity parameter, v_t , that produces no correlation between the strength of Fe I lines and the abundances derived from them. We iterate the calculations for T_{eff} , $\log g$, and v_t with updated $[\text{Fe}/\text{H}]$ values. Departures from LTE (i.e., NLTE) affect the Fe abundance derived from Fe I lines (e.g., [Thévenin & Idiart 1999](#)). We use the INSPECT database¹⁴ ([Bergemann et al. 2012](#); [Lind et al. 2012](#)) to compute NLTE corrections for 15 Fe I lines included in that database. These corrections, listed in Table 2, average $+0.19 \pm 0.01$ dex. This value is in excellent agreement with the empirical correction predicted by equation 1 of [Ezzeddine et al. \(2017\)](#), $+0.18$ dex. The NLTE-corrected $[\text{Fe}/\text{H}]$ ratio derived from Fe I lines is -2.20 ± 0.12 . The $[\text{Fe}/\text{H}]$ ratio derived from Fe II lines, which should be minimally affected by NLTE, is -2.25 ± 0.06 . The two values are in excellent agreement, and we adopt $[\text{Fe}/\text{H}] = -2.20 \pm 0.12$ as the metallicity of J2213–5137.

Table 2. Line Atomic Data and Derived Abundances

Species	λ (Å)	E.P. (eV)	$\log(gf)$	$\log(gf)$ ref.	EW (mÅ)	U.L. flag	$\log \varepsilon$ [LTE]	NLTE corr.
Li I	6707.80	0.00	0.17	1		<	0.70	
O I	7771.94	9.15	0.35	2	20.5		7.32	-0.14
O I	7774.17	9.15	0.20	2	15.9		7.32	-0.14
O I	7775.39	9.15	-0.02	2	13.2		7.44	-0.14
Na I	5889.95	0.00	0.11	3	187.8		4.62	-0.68
Na I	5895.92	0.00	-0.19	3	168.6		4.65	-0.63

Table 2 continued

¹⁴ <http://www.inspect-stars.com>

Table 2 (continued)

Species	λ	E.P.	$\log(gf)$	$\log(gf)$	EW	U.L.	$\log \varepsilon$	NLTE
	(Å)	(eV)		ref.	(mÅ)	flag	[LTE]	corr.

NOTE—The NLTE-corrected abundances may be obtained by adding the NLTE corrections to the LTE $\log \varepsilon$ abundances. The complete version of Table 2 is available in machine-readable form in the online edition of the journal. A portion is shown here to illustrate its form and content.

References—1: Smith et al. (1998), using HFS from Kurucz (2011); 2: Magg et al. (2022); 3: Kramida et al. (2021) (NIST ASD); 4: Pehlivan Rhodin et al. (2017); 5: Kramida et al. (2021), using HFS from VALD3 (Piskunov et al. 1995; Pakhomov et al. 2019); 6: Den Hartog et al. (2021); 7: Lawler & Dakin (1989), using HFS from Kurucz (2011); 8: Lawler et al. (2013); 9: Wood et al. (2013); 10: Lawler et al. (2014), including HFS; 11: Wood et al. (2014a), including HFS; 12: Sobeck et al. (2007); 13: Lawler et al. (2017); 14: Den Hartog et al. (2011), including HFS; 15: O’Brian et al. (1991); 16: Belmonte et al. (2017); 17: Den Hartog et al. (2014); 18: Ruffoni et al. (2014); 19: Meléndez & Barbuy (2009); 20: Den Hartog et al. (2019); 21: Lawler et al. (2015), including HFS; 22: Wood et al. (2014b); 23: Kramida et al. (2021), using HFS from Kurucz (2011); 24: Roederer & Lawler (2012); 25: Li et al. (1999); 26: Morton (2000); 27: Biémont et al. (2011); 28: Ljung et al. (2006); 29: Nilsson et al. (2010); 30: Wickliffe et al. (1994); 31: Duquette & Lawler (1985); 32: Biémont et al. (1982); 33: Hansen et al. (2012), including HFS and IS; 34: Kramida et al. (2021), using HFS/IS from McWilliam (1998) when available; 35: Lawler et al. (2001a), using HFS from Ivans et al. (2006) when available; 36: Lawler et al. (2009); 37: Li et al. (2007), using HFS from Sneden et al. (2009); 38: Ivarsson et al. (2001), using HFS from Sneden et al. (2009); 39: Den Hartog et al. (2003), using HFS and IS from Roederer et al. (2008) when available; 40: Lawler et al. (2006), using HFS and IS from Roederer et al. (2008) when available; 41: Lawler et al. (2001c), using HFS and IS from Ivans et al. (2006); 42: Den Hartog et al. (2006); 43: Lawler et al. (2001b), using HFS from Lawler et al. (2001d); 44: Wickliffe et al. (2000); 45: Lawler et al. (2004), including HFS; 46: Lawler et al. (2008); 47: Wickliffe & Lawler (1997); 48: Sneden et al. (2009), including HFS and IS; 49: Lawler et al. (2009), including HFS; 50: Lawler et al. (2007); 51: Quinet et al. (2006); 52: Xu et al. (2007), using HFS and IS from Cowan et al. (2005); 53: Den Hartog et al. (2005), including HFS and IS; 54: Biémont et al. (2000), including HFS and IS from Roederer et al. (2012); 55: Nilsson et al. (2002b); 56: Nilsson et al. (2002a).

3.2. Abundance Analysis

We measure EWs for O I, Na I, Mg I, Si I, K I, Ca I, Ti I and II, Cr I and II, Ni I, and Zn I using the same methods described in Section 3.1. We derive abundances from these EWs using the MOOG “abfind” driver, the model atmosphere derived in Section 3.1, and the atomic data presented in Table 2. We derive abundances or upper limits for all other species using the MOOG “synth” driver. We generate line lists for the synthetic spectrum matching using the LINEMAKE code¹⁵ (Placco et al. 2021). We include multiple isotopes in our syntheses for the elements Li (${}^6\text{Li}/{}^7\text{Li} = 0$; Lind et al. 2013), C (${}^{12}\text{C}/{}^{13}\text{C} = 5$, typical for an evolved star; Gratton

et al. 2000), N (${}^{15}\text{N}/{}^{14}\text{N} = 0$; Meija et al. 2016), Cu (${}^{63}\text{Cu}/{}^{65}\text{Cu} = 2.24$, the Solar ratio; Meija et al. 2016), Ag, Ba, Nd, Sm, Eu, Yb, Ir, Pt, and Pb. We adopt the r -process isotopic ratios for Ag through Pb (Sneden et al. 2008). We apply NLTE corrections for lines of O I (Amarsi et al. 2015), Na I (Lind et al. 2011), Al I (Nordlander & Lind 2017; Roederer & Lawler 2021), K I (Takeda et al. 2002), Ti I (Bergemann 2011), Cu I (Roederer & Barklem 2018; Shi et al. 2018), and Pb I (Mashonkina et al. 2012; Roederer et al. 2020).

Whenever possible, we derive abundances from features with $\lambda < 3640 \text{ \AA}$ or $\lambda > 4400 \text{ \AA}$, where the density of lanthanide lines is lower and absorption from the convergence of Balmer-series transitions does not complicate continuum identification or modeling. 516 lines in our spectrum of J2213–5137 yield reliable estimates of the abundances (and upper limits) of 47 (53) elements,

¹⁵ <https://github.com/vmplacco/linemake>

including 29 (33) elements produced by r -process nucleosynthesis. Table 3 lists the final abundances, including NLTE corrections.

We compute abundance uncertainties by resampling the model atmosphere parameters and line data 10^3 times, following the method outlined in Roederer et al. (2018b). We conservatively assume that the systematic uncertainties in T_{eff} and $\log g$ may be twice the size of the lower limits adopted in Section 3.1. We also conservatively assume a minimum uncertainty, σ_{EW} , of 2 mÅ and 1% in the EWs of lines, as follows: $\sigma_{\text{EW}} = \sqrt{2.0^2 + (0.01 \times \text{EW})^2}$, where all units are in mÅ. This component accounts for sources of uncertainty that are relatively uniform throughout the spectrum, such as flat-fielding errors, and the values adopted are based on our experience with the data. Our calculations include a wavelength-dependent term that varies smoothly from blue to red to account for S/N and continuum placement, $\sigma_{\text{EW}} = 2 \times 10^{15} \lambda^{-4.2}$, where λ is measured in Å and σ_{EW} is measured in mÅ. These values are also based on our experience with the data. This component of the uncertainty is ≈ 3 mÅ at 3400 Å, ≈ 1.5 mÅ at 4000 Å, and < 1 mÅ at $\lambda > 4400$ Å. We add these two components of the uncertainty in quadrature. We compute the unweighted mean abundance of each element, X , and the $[X/\text{Fe}]$ ratio for each resample. The uncertainties listed in Table 3 reflect the inner 68th percentiles of the distributions.

Figures 2–4 show fits to several lines of interest. There are large changes to the synthetic spectra induced by changes of ± 0.3 dex in the input abundance, demonstrating that most of these lines are on the linear part of the curve-of-growth. The profile exhibited by lines of La II, Ho II, and Lu II is non-Gaussian. The seven hyperfine components of the Lu II $\lambda 5983$ line, for example, span ≈ 0.68 Å. Our synthetic line component pattern is based on the data presented in Lawler et al. (2009), and it provides a satisfactory fit to the observed spectrum. It is rare for Th II lines, other than the one at 4019 Å, to be detectable. Eight Th II lines are reliable abundance indicators in J2213–5137, and four are shown in Figures 2–4. Finally, we detect the U II line at 3859 Å, as shown in Figure 3, marking just the eighth time that uranium has been detected in an r -process-enhanced star.

3.3. Kinematics

We compute the kinematic and orbital properties of J2213–5137. We adopt the astrometric data from Gaia DR3 and the radial velocity from our MIKE spectra. We assume that the position and velocity of the Sun are $(x, y, z)_{\odot} = (-8.178, 0, 0)$ kpc (GRAVITY Collaboration et al. 2019) and $(v_x, v_y, v_z)_{\odot} = (11.10, 247.30, 7.25)$ km s⁻¹ (Reid & Brunthaler 2004). We draw 10^5 samples of the phase-space information $(\varpi, \alpha, \delta, v_r, \mu_{\alpha*}, \mu_{\delta})$ from their associated error distributions, neglecting the tiny observational uncertainty

Table 3. Derived Abundances

Species	Z	$\log \varepsilon_{\odot}$	$\log \varepsilon(X)$	$[X/\text{Fe}]^a$	$\sigma(\log \varepsilon(X))$	$\sigma([X/\text{Fe}])$	N
Li I	3	...	<0.70	1
C (CH)	6	8.43	6.61	+0.38	0.30	0.30	1
N (NH)	7	7.83	<6.30	< +0.67	1
O I	8	8.69	7.22	+0.73	0.15	0.26	3
Na I	11	6.24	3.98	-0.06	0.17	0.07	2
Mg I	12	7.60	5.89	+0.49	0.11	0.05	4
Al I	13	6.45	3.87	-0.38	0.17	0.08	1
Si I	14	7.51	5.63	+0.32	0.20	0.22	4
Si II	14	7.51	5.70	+0.39	0.17	0.19	2
K I	19	5.03	2.98	+0.15	0.11	0.04	2
Ca I	20	6.34	4.39	+0.25	0.09	0.05	17
Sc II	21	3.15	1.08	+0.13	0.08	0.07	3
Ti I	22	4.95	3.13	+0.38	0.15	0.06	10
Ti II	22	4.95	3.02	+0.27	0.07	0.06	4
V I	23	3.93	1.82	+0.09	0.17	0.08	2
V II	23	3.93	1.85	+0.12	0.14	0.13	3
Cr I	24	5.64	3.18	-0.26	0.14	0.06	4
Cr II	24	5.64	3.46	+0.02	0.10	0.10	2
Mn I	25	5.43	2.88	-0.35	0.20	0.14	3
Mn II	25	5.43	2.86	-0.37	0.12	0.11	1
Fe I	26	7.50	5.30	-2.20	0.12	0.12	99
Fe II	26	7.50	5.25	-2.25	0.06	0.06	11
Co I	27	4.99	2.66	-0.13	0.22	0.12	7
Ni I	28	6.22	3.90	-0.12	0.11	0.06	12
Cu I	29	4.19	1.22	-0.77	0.22	0.12	1
Zn I	30	4.56	2.52	+0.16	0.10	0.07	2
Ge I	32	3.65	<2.40	< +0.95	1
Rb I	37	2.52	<2.20	< +1.88	1
Sr II	38	2.87	1.79	+1.12	0.18	0.18	2
Y II	39	2.21	1.14	+1.13	0.08	0.07	23
Zr II	40	2.58	1.87	+1.49	0.09	0.08	9
Nb II	41	1.46	0.90	+1.64	0.18	0.18	3
Mo I	42	1.88	1.34	+1.66	0.27	0.20	2
Ru I	44	1.75	1.59	+2.04	0.19	0.08	4
Rh I	45	0.91	0.99	+2.28	0.23	0.13	3
Pd I	46	1.57	1.15	+1.78	0.21	0.10	3
Ag I	47	0.94	0.50	+1.76	0.22	0.12	1
Ba II	56	2.18	1.70	+1.72	0.13	0.12	6
La II	57	1.10	0.87	+1.97	0.11	0.10	24
Ce II	58	1.58	1.07	+1.69	0.10	0.09	19
Pr II	59	0.72	0.47	+1.95	0.11	0.10	9
Nd II	60	1.42	1.15	+1.93	0.11	0.10	43
Sm II	62	0.96	0.93	+2.17	0.11	0.10	38
Eu II	63	0.52	0.77	+2.45	0.09	0.08	10
Gd II	64	1.07	1.12	+2.25	0.12	0.10	34
Tb II	65	0.30	0.29	+2.19	0.13	0.11	5
Dy II	66	1.10	1.24	+2.34	0.16	0.15	15
Ho II	67	0.48	0.46	+2.18	0.16	0.14	8
Er II	68	0.92	1.03	+2.31	0.13	0.12	11
Tm II	69	0.10	0.12	+2.22	0.12	0.11	9
Yb II	70	0.84	1.01	+2.37	0.20	0.19	1
Lu II	71	0.10	0.36	+2.46	0.08	0.07	4
Hf II	72	0.85	0.71	+2.06	0.12	0.11	5
Os I	76	1.40	1.60	+2.40	0.24	0.12	2
Ir I	77	1.38	1.45	+2.27	0.21	0.10	2
Pt I	78	1.62	<1.95	< +2.53	1
Pb I	80	2.04	<1.50	< +1.66	2
Th II	90	0.02	0.22	+2.40	0.13	0.12	8
U II	92	-0.54	-0.74	+2.00	0.26	0.26	1

^a $[\text{Fe}/\text{H}]$ is given instead of $[X/\text{Fe}]$ for Fe.

NOTE—The Solar abundances, listed in column 3, are adopted from Asplund et al. (2009). The abundance of element X is defined as the number of X atoms per 10^{12} H atoms, $\log \varepsilon(X) \equiv \log_{10}(N_X/N_H) + 12.0$. The C abundances have been corrected (by +0.71 dex) to the “natal” abundance according to the stellar evolution corrections presented by Placco et al. (2014). A single C abundance is derived by synthesizing the CH molecular features in the spectral region from 4290–4330 Å. A single N abundance is derived by synthesizing the NH molecular features in the spectral region from 3360–3370 Å. NLTE corrections have been applied to the abundances derived from O I, Na I, Al I, K I, Ti I, and Fe I lines.

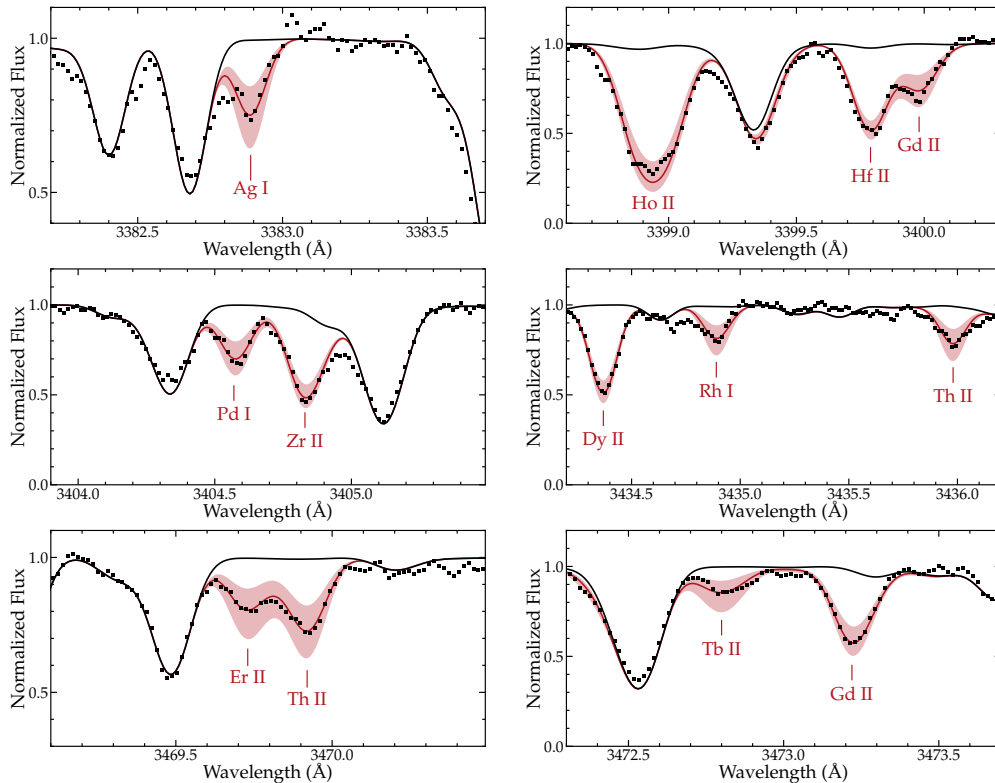


Figure 2. Comparison of observed spectra (black dots) and synthetic spectra for several lines of interest. The red line marks the best-fit abundance to each absorption line, and the light red band marks ± 0.3 dex relative to the best-fit line. The black lines are synthesized without the element of interest.

in (α, δ) . We apply a correction for the zero-point offset in parallax¹⁶, and we account for the correlated observational uncertainties in $(\varpi, \mu_{\alpha*}, \mu_{\delta})$.

We convert these quantities into position and velocity vectors in Galactocentric Cartesian coordinates, $\mathbf{x} = (x, y, z)$ and $\mathbf{v} = (v_x, v_y, v_z)$, in the same manner as Hattori et al. (2023). We derive the kinematic properties of J2213–5137 using the AGAMA package (Vasiliev 2019). We calculate the orbital action $\mathbf{J} = (J_r, J_z, J_\phi)$ and energy $E = \frac{1}{2}v^2 + \Phi_{\text{MW}}(\mathbf{x})$ using (\mathbf{x}, \mathbf{v}) and adopting the gravitational potential model of the Milky Way, Φ_{MW} , from McMillan (2017). We define $J_\phi = Rv_\phi = -(xv_y - yv_x)$, so that stars with prograde orbits have $J_\phi > 0$ and $v_\phi > 0$. For each realization of (\mathbf{x}, \mathbf{v}) , we integrate the orbit forward in time steps of 1 Myr for 100 Gyr, which is more than sufficient to characterize the orbital properties. We use these integrations to derive the orbital pericentric radius (r_{peri}), orbital apocentric radius (r_{apo}), maximum excursion above or below the Galactic plane (z_{max}), and orbital eccentricity (e),

defined as $(r_{\text{apo}} - r_{\text{peri}})/(r_{\text{apo}} + r_{\text{peri}})$. Table 1 summarizes the orbital properties of this star.

4. RESULTS

The abundance ratios among the light elements ($Z \leq 30$) in J2213–5137 are typical for stars with $[\text{Fe}/\text{H}] = -2.2$. We briefly summarize these results, and we refer readers to numerous other studies that interpret them in terms of stellar evolution, stellar nucleosynthesis, and Galactic chemical evolution. Lithium (Li, $Z = 3$) is undetected. Carbon (C, $Z = 6$) and nitrogen (N, $Z = 7$) are not present at levels that would be considered enhanced. The α elements O, Mg, Si, Ca, and Ti ($Z = 8, 12, 14, 20,$ and 22 , respectively) are enhanced relative to Fe (Fe, $Z = 26$), $[\alpha/\text{Fe}] = +0.38 \pm 0.07$. The ratios of the odd- Z elements sodium, aluminum, and potassium (Na, Al, and K; $Z = 11, 13,$ and 19 , respectively) to Fe are Solar to within a factor of ≈ 3 . The iron-group elements scandium, vanadium, chromium, cobalt, nickel, and zinc (Sc, V, Cr, Co, Ni, and Zn; $Z = 21, 23, 24, 27, 28,$ and 30 , respectively) are also present in scaled-Solar proportions. Only the elements manganese (Mn, $Z = 25$) and copper (Cu, $Z = 29$) are present in sub-Solar abundance ratios, $[\text{Mn}/\text{Fe}] = -0.37 \pm 0.11$ and $[\text{Cu}/\text{Fe}] = -0.72 \pm 0.12$.

¹⁶ We use a package provided by Gaia Data Processing and Analysis Consortium (DPAC), available at https://gitlab.com/icc-ub/public/gaiadr3_zero_point, to obtain the parallax zero-point offset, -0.03251 mas.

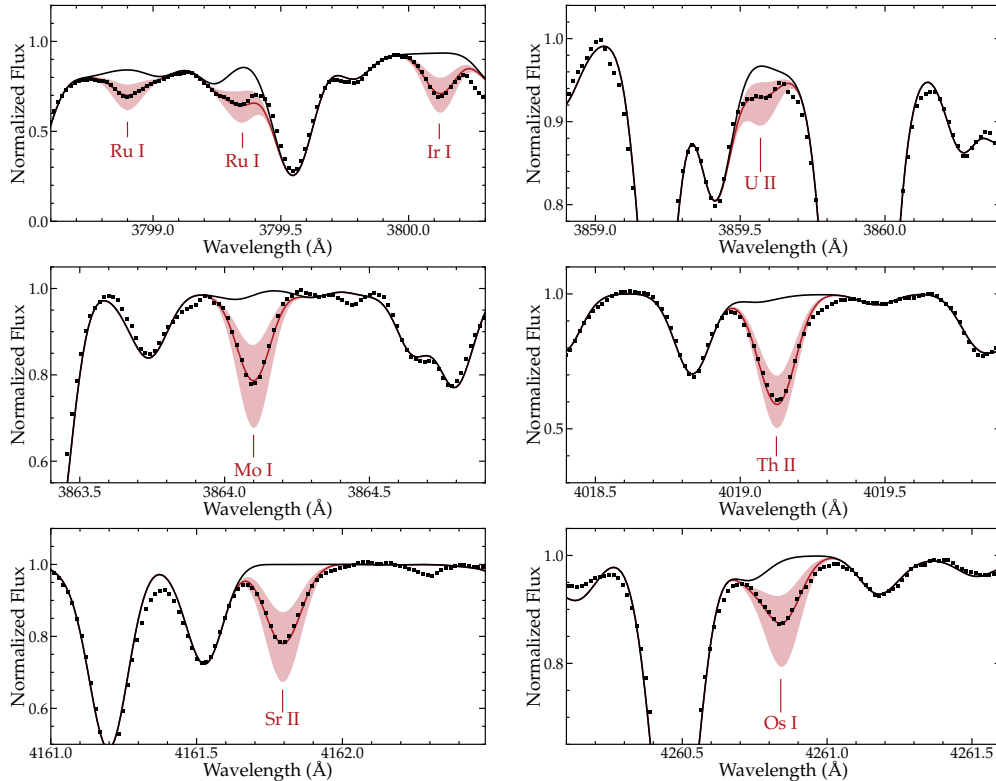


Figure 3. Comparison of observed and synthetic spectra for several lines of interest. Symbols are the same as in Figure 2.

We detect 29 heavy elements and derive upper limits on the abundances of four other heavy elements not detected in our spectrum of J2213–5137. Figure 5 shows the heavy-element abundance pattern of J2213–5137. The calculated slow neutron-capture process (*s*-process) contribution to the Solar System and the inferred Solar *r*-process residuals are shown for comparison. The Solar *r*-process pattern provides an excellent fit to the heavy-element abundance pattern of J2213–5137, whereas the *s*-process one does not. The Solar *r*-process pattern and the J2213–5137 pattern match to within $\approx 2\sigma$, and often much better, for the elements with $56 \leq Z \leq 82$. The deviations for Th and U ($Z = 90$ and 92) are due to their longer radioactive decay ages relative to the age of the actinides in the Solar System (see Sections 5.2 and 5.3). The lighter *r*-process elements with $38 \leq Z \leq 47$ exhibit a poor match to both patterns, and we discuss these elements separately in Sections 5.1 and 5.4. J2213–5137 exhibits $[\text{Eu}/\text{Fe}] = +2.45 \pm 0.08$ and $[\text{Ba}/\text{Eu}] = -0.73 \pm 0.14$, identifying it as a member of the class of *r*-III stars proposed by Cain et al. (2020).

5. DISCUSSION

5.1. No Contamination from Other Processes

Other nucleosynthesis processes could, in principle, contribute to the heavy-element abundance patterns in stars with $[\text{Fe}/\text{H}] > -2.6$ or so (Simmerer et al. 2004).

In this section, we present evidence that any such contamination to J2213–5137 is minimal.

Three well-studied *r*-II stars are shown in Figure 6 for comparison. They have been selected to span a range of metallicities and $[\text{Eu}/\text{Fe}]$ ratios within the *r*-II class. CS 22892-052 was the first such star identified (Snedden et al. 1994). It exhibits $[\text{Fe}/\text{H}] = -3.12$ and $[\text{Eu}/\text{Fe}] = +1.65$ (Snedden et al. 2003, 2009). BD +17°3248 exhibits a metallicity similar to J2213–5137, $[\text{Fe}/\text{H}] = -2.10$ (Cowan et al. 2002). Its $[\text{Eu}/\text{Fe}]$ ratio is near the low end for *r*-II stars, at $+0.90$. HD 222925 is also shown in Figure 6. Its metallicity, $[\text{Fe}/\text{H}] = -1.46$, is considerably higher than that of J2213–5137, while its $[\text{Eu}/\text{Fe}]$ ratio is $+1.32$ (Roederer et al. 2022a).

Figure 6 demonstrates that there are no discernible differences among the heavy *r*-process elements and some of the lighter *r*-process elements in these four stars. Differences among the lighter *r*-process elements may only be apparent for the elements Ru, Rh, Pd, and Ag ($44 \leq Z \leq 47$). Roederer et al. (2023) identified these four elements as being produced, in part, as fission fragments of transuranic elements. Otherwise, the similarity among these abundance patterns across a range of metallicities and levels of *r*-process enhancement reinforces two key ideas. First, these elemental mass ranges appear to exhibit abundance universality (Snedden et al. 2009; Roederer et al. 2022b), provided the light and heavy elements are normalized separately.

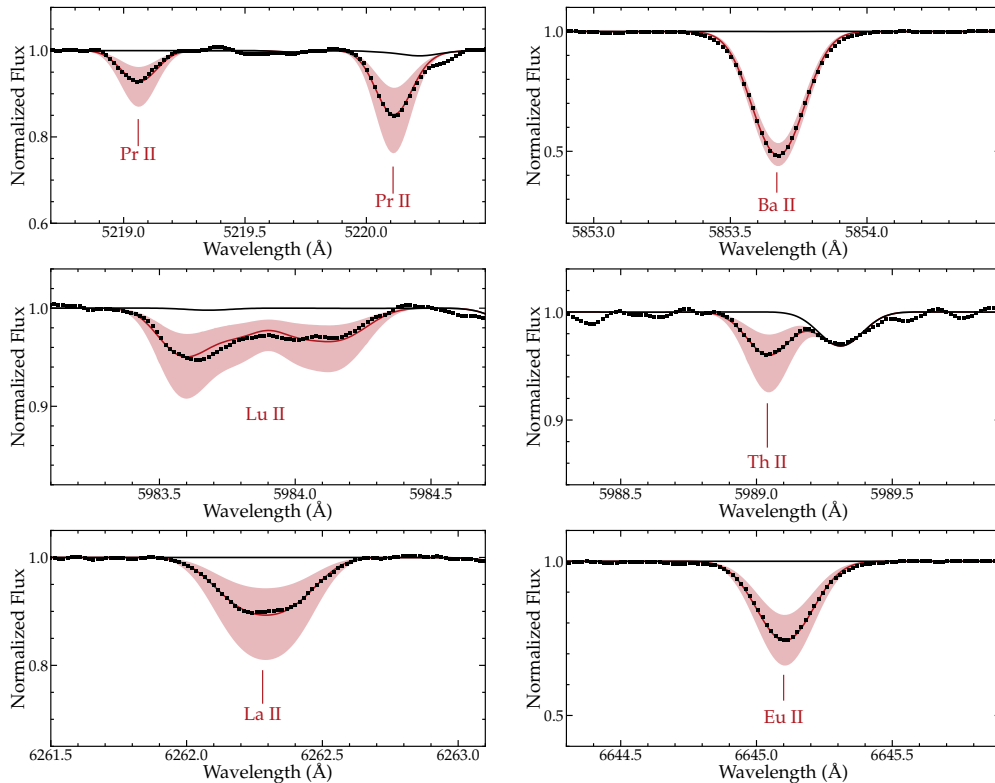


Figure 4. Comparison of observed spectra (black dots) and synthetic spectra for several lines of interest. Symbols are the same as in Figure 2.

Secondly, contamination from other nucleosynthesis processes, such as charged-particle reactions or s -process nucleosynthesis, is minimal. Even in relatively metal-rich stars, such as J2213–5137, BD +17°3248, or even HD 222925, the r -process dominates the abundance patterns.

5.2. Detection of Thorium and Uranium

We detect the actinide elements thorium (Th, $Z = 90$) and uranium (U, $Z = 92$) in J2213–5137. Th II lines have been detected previously in several dozen r -process-enhanced stars (e.g., Johnson & Bolte 2001; Honda et al. 2004; Ren et al. 2012). The strongest U II lines are weaker than the strongest Th II lines, and U has only been detected in seven r -process-enhanced stars previously (Cayrel et al. 2001; Hill et al. 2002, 2017; Cowan et al. 2002; Frebel et al. 2007; Placco et al. 2017; Holmbeck et al. 2018; Yong et al. 2021).

We derive the Th abundance of J2213–5137 from eight Th II lines. Several of these lines are shown in Figures 2–4. These lines all yield concordant abundances.

We detect the strongest optical U II line at 3859.57 Å, as shown in Figure 3. Shah et al. (2023) reanalyzed this line in four stars with previous U detections and found that it yields concordant abundances with two additional U II lines, at 4050.04 Å and 4090.13 Å. In J2213–5137, U II accounts for less than $\approx 5\%$ of the

absorption at the $\lambda 4050$ line, which is highly blended with a La II line. The U II $\lambda 4090$ line is blended with an Fe I line, and the total absorption depth is less than 2% of the continuum. Continuum placement is uncertain by at least 1% in this region. Potential U II absorption at 4241.66 Å is also coincident with a Zr I line of uncertain strength. Upper limits derived from these U II lines and four others that are too weak to detect (Table 2) are consistent with the U abundance derived from the $\lambda 3859$ line.

Table 4 (column 2) lists the $\log \varepsilon(\text{Th}/\text{Eu})$, $\log \varepsilon(\text{U}/\text{Eu})$, and $\log \varepsilon(\text{U}/\text{Th})$ abundance ratios derived from our spectrum of J2213–5137. Eu is traditionally preferred as a stable reference element, because its production is also dominated by the r -process and it is readily observable in metal-poor stars. Table 4 (columns 3–5) lists the individual components of the observational uncertainties. The dominant source of uncertainty is the fitting uncertainty, σ_{fit} , which accounts for the S/N, continuum placement, and blending features. Uncertainties in the model atmosphere, σ_{atm} , translate to only small abundance uncertainties when ratios among these elements are considered, because the abundances are derived from lines that respond similarly to changes in the model atmosphere parameters. Uncertainties arising from the $\log(gf)$ values, $\sigma_{\log gf}$, are virtually negligible, thanks to extensive laboratory

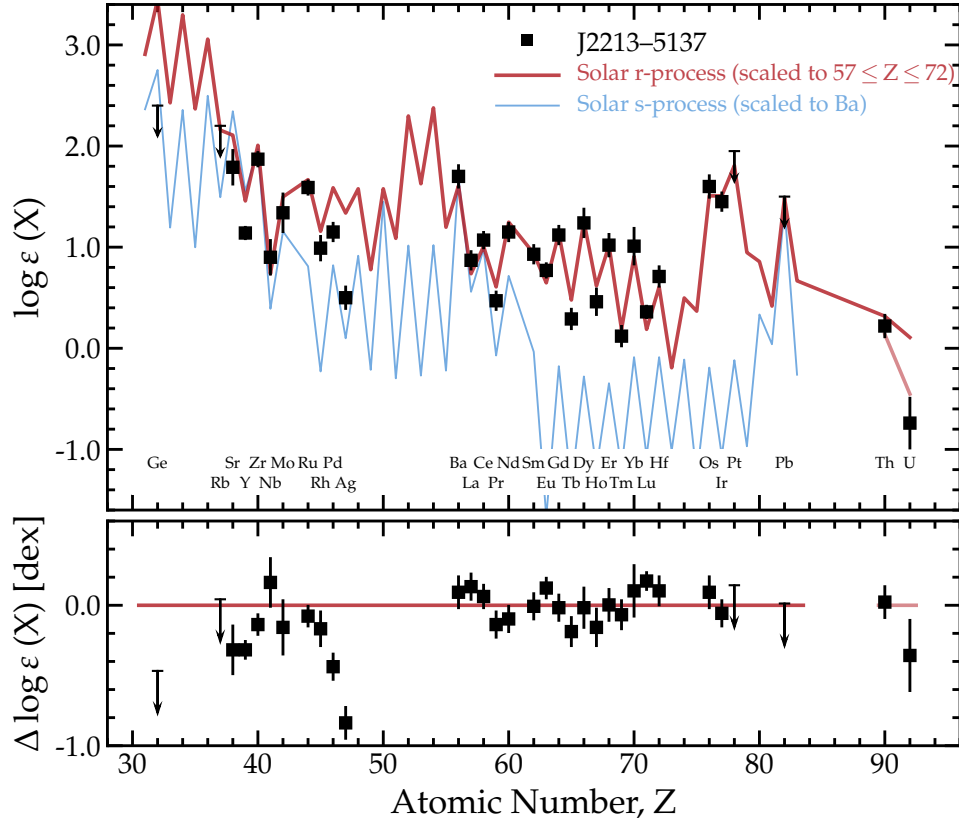


Figure 5. The heavy-element abundance pattern in J2213–5137. Detections are shown as black squares, and upper limits are shown as downward-facing arrows. The top panel compares the stellar pattern with the calculated Solar System s -process pattern and the inferred Solar System r -process residual pattern (Sneden et al. 2008, except for Y, which is adopted from Bisterzo et al. 2014, and Th and U, which are adopted from Lodders 2003). The s -process pattern is normalized to the Ba abundance, and the r -process pattern is normalized to the average abundances of elements from Ba through Hf. The light red line connecting Th and U accounts for 13 Gyr of radioactive decay, which includes an additional 8.5 Gyr relative to the Solar abundances. The bottom panel shows the differences relative to the scaled r -process pattern.

efforts in the last few decades (Lawler et al. 2001c; Nilsson et al. 2002a,b; Ivans et al. 2006). The total uncertainties (column 6) account for the abundance covariances, which we calculate using the Monte Carlo resampling method described in Section 3.2, and these covariances are the reason that the total uncertainties are smaller than those listed in Table 3.

J2213–5137 exhibits no peculiar behavior among its actinide-element abundances. It does not exhibit a so-called “actinide boost” (Hill et al. 2002; Schatz et al. 2002). Its $\log \varepsilon(\text{Th}/\text{Eu})$ ratio is low, -0.55 ± 0.08 , and within the range of most other r -process-enhanced metal-poor stars (e.g., Sneden et al. 2008; Holmbeck et al. 2018), including the r -III star studied by Cain et al. (2020). In contrast, CS 31082-001, the original actinide-boost star, exhibits $\log \varepsilon(\text{Th}/\text{Eu}) = -0.26 \pm 0.14$ (Siqueira Mello et al. 2013). We conclude that the Th and U abundances in J2213–5137 are typical among r -process-enhanced stars.

5.3. Nuclear Chronometers

The age of the r -process material can be calculated from the radioactive decay of the long-lived ^{232}Th ($t_{1/2} = 14.0$ Gyr), ^{235}U ($t_{1/2} = 0.704$ Gyr), and ^{238}U ($t_{1/2} = 4.468$ Gyr) isotopes (Fowler & Hoyle 1960). These isotopes can only be produced by r -process nucleosynthesis. The radioactive decay of ^{232}Th , ^{235}U , and ^{238}U feeds decay chains that terminate at ^{208}Pb , ^{207}Pb , and ^{206}Pb , respectively. As the Th and U abundances decrease, the Pb abundance increases. After 13 Gyr, the Pb abundance will increase by ≈ 0.10 dex (Roederer et al. 2009). If the s -process contribution to Pb is negligible, then ratios among Pb/Eu, Pb/Th, and Pb/U can also be used to calculate the age (Clayton 1964).

This method can be applied when production of the r -process material was dominated by a single event (e.g., Cowan et al. 1997, 1999; Cayrel et al. 2001). Otherwise, a chemical evolution model is required (e.g., Thielemann et al. 1983; Cowan et al. 1987; Mathews & Schramm 1988). The high level of r -process enhancement leaves little doubt that the single-event scenario can be ap-

Table 4. Eu, Pb, Th, and U Abundance Ratios: Uncertainties, Production Ratios, and Inferred Ages

(1)	(2)	(3)	(4)	(5)	(6)	(7)	(8)	(9)	(10)	(11)	(12)	(13)	(14)	(15)	(16)
$\log \varepsilon(X)$	Value	$\sigma_{\log gf}$	σ_{atm}	σ_{fit}	σ_{total}	Production Ratios				Age				$\sigma_{\text{age, PR}}$	$\sigma_{\text{age, obs}}$
						C02	S02	K07	H17	C02	S02	K07	H17		
Th/Eu	−0.55	0.01	0.04	0.06	0.08	−0.29	−0.33	−0.34	−0.24	12.0	10.3	9.9	14.6	4.5	3.7
U/Eu	−1.51	0.05	0.04	0.15	0.16	−0.55	−0.55	−0.54	−0.52	14.2	14.1	14.4	14.7	1.5	2.4
U/Th	−0.96	0.05	0.01	0.15	0.16	−0.26	−0.22	−0.20	−0.28	15.1	16.2	16.5	14.8	2.2	3.5
Pb/Eu	<0.73	0.61	(any)
Pb/Th	<1.28	0.95	<11.6	...	4.3	...
Pb/U	<2.24	0.81	<14.2	...	1.5	...
Mean										13.8	13.5	13.6	14.7		

NOTE—All ages are reported in units of Gyr. $\sigma_{\text{age, PR}}$ is the component of the age uncertainty due to an uncertainty in the log of the production ratio of 0.1 dex ($\approx 20\%$). $\sigma_{\text{age, obs}}$ is the component of the age uncertainty due to observational uncertainties (column 6).

References—C02 = Cowan et al. (2002), based on Cowan et al. (1999); S02 = Schatz et al. (2002); K07 = Kratz et al. (2007), “fit2”, including Pb predictions from Roederer et al. (2009); H17 = Hill et al. (2017).

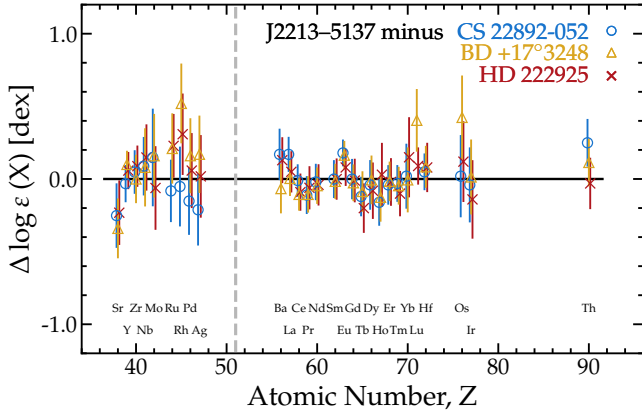


Figure 6. Comparison of the heavy-element abundance pattern in J2213–5137 with three other well-studied r -II stars. The differences for the elements with $Z \geq 56$ are normalized to the lanthanide elements and their immediate neighbors ($56 \leq Z \leq 72$), and the differences for the elements with $Z \leq 47$ are normalized to the elements with $38 \leq Z \leq 42$. The vertical dashed gray line divides these two mass ranges, and the horizontal black line indicates a difference of zero. The points are offset slightly in the horizontal direction to improve clarity. References are given in Section 5.1.

plied to J2213–5137. A modest amount of caution is appropriate, however, because previous studies of a few actinide boost stars have found that the levels of the actinide elements can be so enhanced that this method

returns negative, non-physical ages (e.g., Hill et al. 2002; Mashonkina et al. 2014), and there are hints of a potential metallicity dependence (Saraf et al. 2023).

This method also requires that the initial production ratios are known. Table 4 (columns 7–10) lists the production ratios predicted by several methods. These calculations are frequently tuned to reproduce the Solar System r -process isotopic component, so they are not independent, but their range provides an estimate of their level of uncertainty. The predicted initial production ratios are also sensitive to the choice of nuclear physics inputs and the r -process model (e.g., Cowan et al. 1999; Holmbeck et al. 2019). Schatz et al. (2002) estimated that the uncertainties in the production ratios may be ≈ 0.10 – 0.12 dex. Table 4 (column 15) lists the component of the age uncertainty that results from an uncertainty of 0.10 dex in the production ratios.

The absolute ages, calculated using equations 1–3 of Cayrel et al. (2001) and Equations A1–A5 in Appendix A, are listed in Table 4 (columns 11–14). Table 4 (column 16) lists the component of the age uncertainty that results from the observational uncertainty in each abundance ratio (Section 5.2). We resample the observed abundances and the production ratios and compute the mean of the resulting age distributions. These values, which range from 13.5 Gyr to 14.7 Gyr for different sets of production ratios, are listed in the bottom row of Table 4. Their uncertainties, computed from the 16th and 84th percentiles of the distributions, are ≈ 2.6 Gyr.

The Pb abundance in J2213–5137 is an upper limit only, so the ages predicted from ratios involving the ra-

diogenic production of Pb through actinide decay are also upper limits. These limits are consistent with the ages derived from the Th/Eu, U/Eu, and U/Th ratios. Detecting the Pb II line at 2203 Å, which should be strong in J2213–5137, would provide a unique opportunity to calculate ages from both the parent and daughter nuclei in a star where all three abundances are derived from lines of the majority species (Roederer et al. 2020).

Figure 7 compares the predicted abundance ratios involving Eu, Pb, Th, and U with the ratios derived for J2213–5137. To simplify the figure, only one set of predicted production ratios is shown. The age inferred from the Kratz et al. (2007) production ratios, 13.6 ± 2.6 Gyr, is shown by the vertical band in Figure 7.

5.4. Transuranic Fission Fragments

Roederer et al. (2023) noticed that the $\log \varepsilon(\text{Ru}/\text{Zr})$, $\log \varepsilon(\text{Rh}/\text{Zr})$, $\log \varepsilon(\text{Pd}/\text{Zr})$, and $\log \varepsilon(\text{Ag}/\text{Zr})$ ratios in r -process-enhanced stars correlated with the $[\text{Eu}/\text{Fe}]$ ratio. That study interpreted those correlations as potential evidence that fission fragments of transuranic elements boosted the production of Ru, Rh, Pd, and Ag in strong r -process events that might produce more Eu, lanthanides, and transuranic elements. Figure 8 shows the relationships between these elements for the sample of stars examined by Roederer et al. J2213–5137 is also shown in Figure 8, and it extends the range of $[\text{Eu}/\text{Fe}]$ ratios to much higher values than were available previously. J2213–5137 does not continue the upward extrapolation of the trends identified by Roederer et al. Instead, J2213–5137 exhibits relative enhancements of Ru, Rh, Pd, and Ag that are similar to those found in stars with $+1.3 \leq [\text{Eu}/\text{Fe}] \leq +1.7$ or so.

Perhaps the fact that these trends do not continue to higher $[\text{Eu}/\text{Fe}]$ ratios suggests that there is a maximum strength of the r -process. For example, there could be a limit on the number of times fission cycling occurs, or there could be a maximum duration of time when the neutron density remains high enough for an r -process. Studying the four key elements—Ru, Rh, Pd, and Ag—in additional r -process-enhanced stars with $[\text{Eu}/\text{Fe}] > +1.7$ will be critical to understand this behavior. Among these elements, only Ru was derived by Cain et al. (2020) for J1521–3538, the r -III star known previously. The high value of its $\log \varepsilon(\text{Ru}/\text{Zr})$ ratio, -0.24 ± 0.24 , is within the same range as found for J2213–5137 and other stars with $[\text{Eu}/\text{Fe}] > +1.3$. Abundances of these elements have not been published for any other r -process-enhanced star with $[\text{Eu}/\text{Fe}] > +1.7$. We predict that r -process-enhanced stars in the Reticulum II dwarf galaxy, which exhibit $[\text{Eu}/\text{Fe}] = +1.69 \pm 0.12$ or $[\text{Eu}/\text{H}] = -0.98 \pm 0.13$ on average (Ji et al. 2016b), should exhibit similarly high $\log \varepsilon(\text{Ru}, \text{Rh}, \text{Pd}, \text{Ag}/\text{Zr})$ ratios.

5.5. A New Method to Estimate the Dilution Mass or r -process Yields

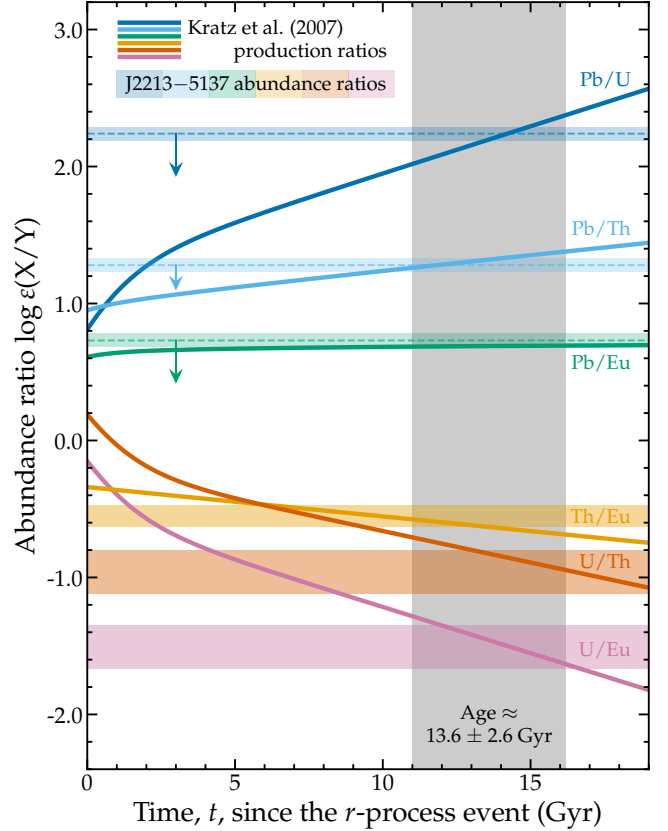


Figure 7. Comparison of observed (shaded horizontal bands) and predicted (solid lines) abundance ratios as a function of age for J2213–5137. The production ratios are drawn from Kratz et al. (2007), supplemented with Pb data presented in Roederer et al. (2009) from the same set of calculations. The $\log \varepsilon(\text{U}/\text{Eu})$ and $\log \varepsilon(\text{U}/\text{Th})$ curves include the $+0.39$ dex contribution from the relatively rapid decay of ^{235}U , which is otherwise not accounted for in equations 2 and 3 of Cayrel et al. (2001). Those equations only accounted for ^{238}U decay, and the $\log \varepsilon(^{238}\text{U}/\text{Eu})$ and $\log \varepsilon(^{238}\text{U}/\text{Th})$ contributions have production ratios of -0.54 and -0.20 , respectively, at time $t = 0$, which are the values listed in Table 4. The equations relating the Pb abundance to age are presented in Appendix A. The age (vertical gray band) is computed based on the Th/Eu, U/Th, and U/Eu ratios.

We propose that the horizontal dispersion of stars around the best-fit fiducial lines in Figure 8 may reflect a combination of dilution into various amounts of Fe in the interstellar medium (ISM) and a range of r -process yields from the events that enriched each of the stars in the sample. We assume that the abundance ratio shown on the vertical axis in each panel is a fixed, intrinsic property of an r -process nucleosynthesis event. If the fiducial line in each panel reveals the average behavior of the sample, then each star’s horizontal displacement in $[\text{Eu}/\text{Fe}]$ reflects the *relative* variation in dilution

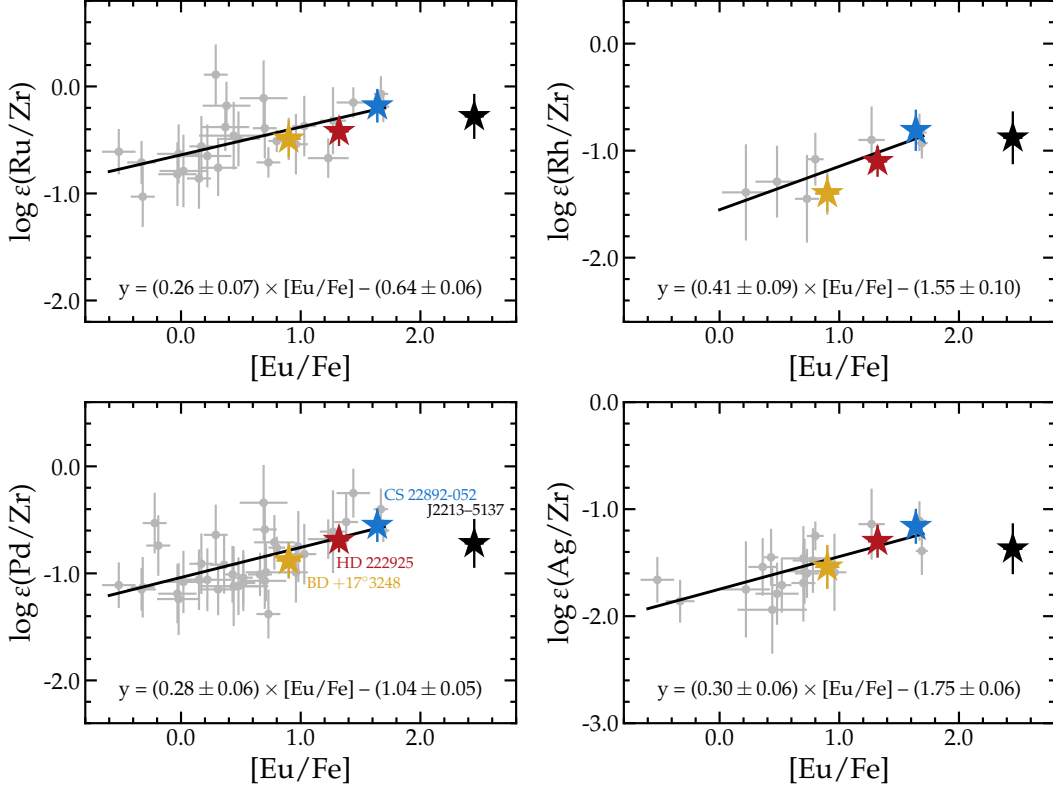


Figure 8. Ratios most affected by fission-fragment distributions for J2213–5137 and the sample of stars studied by Roederer et al. (2023). A few stars are marked in separate colors and labeled individually. The black line marks a best fit to the sample of stars studied by Roederer et al., excluding J2213–5137. The equation for this fiducial line is provided in each panel, where y is shorthand for the $\log \varepsilon(\text{X}/\text{Zr})$ ratio printed on the vertical axis in each panel.

(i.e., the Fe abundance varies) and/or yields (i.e., the Eu abundance varies).

We express the relative displacement in $[\text{Eu}/\text{Fe}]$, δ_{EuFe} , as follows:

$$\begin{aligned} \log \delta_{\text{EuFe}} &= [\text{Eu}/\text{Fe}]_{\text{excess}} \\ &= [\text{Eu}/\text{Fe}]_{\star} - [\text{Eu}/\text{Fe}]_{\text{fiducial}} \\ &= [\text{Eu}/\text{Fe}]_{\star} - (a \log \varepsilon(\text{X}/\text{Zr}) - b)/a. \end{aligned} \quad (1)$$

Here, X is one of the elements that exhibits this behavior: Ru, Rh, Pd, or Ag. The constants a and b are the slope and intercept, respectively, of the best-fit line to the relationships shown in Figure 8, which were derived in Roederer et al. (2023). The dilution and yields are degenerate, so multiple combinations of dilution values and yield variations are permissible. We emphasize that δ_{EuFe} reflects the dilution or r -process yields relative to the rest of the sample; it is not an absolute measure. For example, consider a hypothetical star for which $[\text{Eu}/\text{Fe}]$ is 0.3 dex higher than the fiducial $[\text{Eu}/\text{Fe}]$ ratio that corresponds to the observed $\log \varepsilon(\text{Pd}/\text{Zr})$ ratio. Assume that this r -process material was diluted into an average amount of Fe in the ISM. Equation 1 would thus predict that the r -process event that enriched this star had a yield that was $10^{\delta_{\text{EuFe}}} = 10^{0.3} = 2$ times higher than

an r -process event that enriched an average star in the sample.

We next estimate δ_{EuFe} for J2213–5137. We draw 10^5 resamples from the $[\text{Eu}/\text{Fe}]$, $\log \varepsilon(\text{Zr})$, $\log \varepsilon(\text{Ru})$, $\log \varepsilon(\text{Rh})$, $\log \varepsilon(\text{Pd})$, and $\log \varepsilon(\text{Ag})$ abundances and their uncertainties, as well as the fiducial lines and their uncertainties. For each resample, we compute the $\log \varepsilon(\text{X}/\text{Zr})$ ratios and δ_{EuFe} . The top panel of Figure 9 shows the relative δ_{EuFe} parameters predicted by each of the four abundance ratios. We resample each of these four distributions and compute the mean of those four resamples 10^5 times to estimate the combined relative δ_{EuFe} parameter. That value, $\log \delta_{\text{EuFe}} = +1.04^{+0.30}_{-0.35}$, is precise to within a factor of ≈ 2 . We repeat this set of calculations for 41 stars from Roederer et al. (2023). The results are listed in Table 5 and shown in the bottom panel of Figure 9.

The peaks of the distributions shown in Figure 9 span nearly 3 dex in $\log \delta_{\text{EuFe}}$. In other words, the combined effects of dilution and r -process yields that contributed to this sample of stars span three orders of magnitude. The long tail to low δ_{EuFe} values reflects the large uncertainties in δ_{EuFe} that result from few and uncertain measurements of Ru, Rh, Pd, and Ag in stars with overall low abundances of these elements. J2213–5137 and

Table 5. Relative $\delta_{\text{Eu/Fe}}$ Parameters for 42 Stars, Sorted by Decreasing [Eu/Fe] Ratios

Star	[Eu/Fe]	[Fe/H]	$\log \delta_{\text{Eu/Fe}}$	$\log \delta_{\text{Eu/Fe}}$	$\log \delta_{\text{Eu/Fe}}$	$\log \delta_{\text{Eu/Fe}}$	$\log \delta_{\text{Eu/Fe}}$
			$\log \varepsilon(\text{Ru/Zr})$	$\log \varepsilon(\text{Rh/Zr})$	$\log \varepsilon(\text{Pd/Zr})$	$\log \varepsilon(\text{Ag/Zr})$	combined
2MASS J22132050–5137385	+2.45	–2.20	+1.06 ^{+0.55} _{–0.75}	+0.82 ^{+0.51} _{–0.68}	+1.30 ^{+0.52} _{–0.62}	+1.18 ^{+0.54} _{–0.65}	+1.04 ^{+0.30} _{–0.35}
CS 31082-001	+1.69	–2.90	–0.04 ^{+0.67} _{–0.92}	+0.18 ^{+0.49} _{–0.63}	+0.12 ^{+0.48} _{–0.63}	+0.49 ^{+0.78} _{–0.88}	+0.12 ^{+0.35} _{–0.40}
CS 29497-004	+1.67	–2.84	–0.52 ^{+0.77} _{–1.11}	–0.08 ^{+0.56} _{–0.74}	–0.62 ^{+0.78} _{–1.00}	–0.47 ^{+0.71} _{–0.88}	–0.50 ^{+0.40} _{–0.49}
CS 22892-052	+1.64	–3.09	–0.13 ^{+0.71} _{–0.97}	–0.16 ^{+0.59} _{–0.77}	–0.11 ^{+0.63} _{–0.81}	–0.33 ^{+0.64} _{–0.80}	–0.26 ^{+0.36} _{–0.44}
2MASS J14325334–4125494	+1.44	–2.97	–0.45 ^{+0.69} _{–0.98}	...	–1.38 ^{+0.94} _{–1.20}	...	–0.98 ^{+0.63} _{–0.80}
HE 1219–0312	+1.38	–2.97	–0.48 ^{+0.99} _{–1.17}	...	–0.48 ^{+0.99} _{–1.17}
HD 222925	+1.32	–1.46	+0.47 ^{+0.58} _{–0.71}	+0.22 ^{+0.46} _{–0.56}	+0.07 ^{+0.48} _{–0.59}	–0.18 ^{+0.58} _{–0.70}	+0.10 ^{+0.29} _{–0.34}
2MASS J15383085–1804242	+1.27	–2.09	+0.04 ^{+1.23} _{–1.42}	–0.32 ^{+0.83} _{–0.97}	–0.27 ^{+1.40} _{–1.53}	–0.76 ^{+1.13} _{–1.30}	–0.39 ^{+0.62} _{–0.69}
CS 31078-018	+1.23	–2.84	+1.34 ^{+0.81} _{–0.78}	...	–0.06 ^{+0.71} _{–0.83}	...	+0.63 ^{+0.56} _{–0.58}
CS 22953-003	+1.03	–2.84	–0.02 ^{+1.12} _{–1.26}	...	+0.25 ^{+1.03} _{–1.11}	...	+0.09 ^{+0.78} _{–0.86}
HE 2327–5642	+0.98	–2.79	–0.06 ^{+1.21} _{–1.29}	...	–0.06 ^{+1.21} _{–1.29}
CS 22896-154	+0.96	–2.69	+0.57 ^{+1.12} _{–1.18}	...	+0.78 ^{+1.04} _{–1.06}	+0.42 ^{+1.23} _{–1.26}	+0.58 ^{+0.69} _{–0.70}
BD +17°3248	+0.90	–2.10	+0.32 ^{+0.80} _{–0.88}	+0.54 ^{+0.55} _{–0.59}	+0.33 ^{+0.62} _{–0.68}	+0.20 ^{+0.72} _{–0.78}	+0.33 ^{+0.36} _{–0.38}
HD 221170	+0.80	–2.20	+0.30 ^{+0.46} _{–0.54}	–0.35 ^{+0.66} _{–0.77}	–0.20 ^{+0.43} _{–0.52}	–0.87 ^{+0.54} _{–0.68}	–0.32 ^{+0.29} _{–0.33}
CD –45°3283	+0.78	–0.99	–0.40 ^{+0.95} _{–1.04}	–0.12 ^{+1.04} _{–1.11}	–0.28 ^{+0.73} _{–0.77}
HD 20	+0.73	–1.60	+1.00 ^{+0.64} _{–0.60}	+0.48 ^{+1.04} _{–1.06}	+1.94 ^{+0.96} _{–0.83}	+0.23 ^{+0.79} _{–0.83}	+0.92 ^{+0.45} _{–0.44}
HD 120559	+0.71	–1.31	+0.53 ^{+0.99} _{–1.02}	+0.14 ^{+1.05} _{–1.08}	+0.33 ^{+0.74} _{–0.76}
HD 3567	+0.70	–1.33	+0.81 ^{+0.99} _{–0.98}	–0.27 ^{+1.04} _{–1.12}	+0.26 ^{+0.74} _{–0.75}
BS 17569-049	+0.70	–2.88	–0.26 ^{+1.11} _{–1.26}	...	–0.90 ^{+1.04} _{–1.18}	+0.51 ^{+1.23} _{–1.24}	–0.25 ^{+0.69} _{–0.73}
2MASS J18301354–4555101	+0.69	–3.57	–1.35 ^{+1.39} _{–1.72}	...	–1.81 ^{+1.31} _{–1.54}	...	–1.65 ^{+1.02} _{–1.18}
HD 115444	+0.66	–2.85	+0.55 ^{+0.76} _{–0.77}	...	+0.55 ^{+0.76} _{–0.77}
HD 186478	+0.52	–2.60	+0.52 ^{+0.95} _{–0.95}	+0.39 ^{+0.88} _{–0.90}	+0.45 ^{+0.66} _{–0.67}
HD 6268	+0.52	–2.63	+0.70 ^{+0.98} _{–0.97}	...	+0.70 ^{+0.98} _{–0.97}
HD 108317	+0.48	–2.37	–0.10 ^{+1.03} _{–1.11}	–0.15 ^{+0.87} _{–0.94}	+0.77 ^{+1.03} _{–1.01}	+0.61 ^{+1.02} _{–1.01}	+0.27 ^{+0.52} _{–0.54}
HD 160617	+0.44	–1.77	–0.26 ^{+1.27} _{–1.38}	...	+0.73 ^{+1.40} _{–1.39}	+1.07 ^{+1.46} _{–1.42}	+0.51 ^{+0.83} _{–0.84}
BD +08°2856	+0.43	–2.11	+0.32 ^{+0.98} _{–0.99}	–0.56 ^{+0.90} _{–0.99}	–0.14 ^{+0.69} _{–0.71}
HD 84937	+0.38	–2.25	–1.39 ^{+0.93} _{–1.20}	–1.39 ^{+0.93} _{–1.20}
HD 19445	+0.37	–2.15	–0.63 ^{+0.91} _{–1.06}	–0.63 ^{+0.91} _{–1.05}
HD 108577	+0.36	–2.36	–0.07 ^{+0.99} _{–1.02}	–0.34 ^{+0.92} _{–0.98}	–0.22 ^{+0.69} _{–0.71}
HD 107752	+0.31	–2.85	+0.78 ^{+1.13} _{–1.07}	...	+0.70 ^{+0.93} _{–0.90}	...	+0.75 ^{+0.76} _{–0.72}
CS 22966-057	+0.29	–2.62	–2.59 ^{+1.20} _{–1.63}	...	–1.15 ^{+1.03} _{–1.15}	...	–1.93 ^{+0.84} _{–1.03}
HD 126238	+0.22	–1.93	+0.25 ^{+1.22} _{–1.21}	–0.17 ^{+1.14} _{–1.19}	+0.29 ^{+1.11} _{–1.10}	+0.22 ^{+1.54} _{–1.56}	+0.14 ^{+0.67} _{–0.67}
HD 2796	+0.17	–2.47	–0.14 ^{+1.14} _{–1.17}	...	–0.29 ^{+1.03} _{–1.09}	...	–0.23 ^{+0.79} _{–0.81}
CS 29518-051	+0.15	–2.69	+1.00 ^{+1.24} _{–1.11}	...	+0.22 ^{+1.06} _{–1.05}	...	+0.62 ^{+0.84} _{–0.79}
HD 85773	+0.02	–2.62	+0.60 ^{+1.43} _{–1.35}	...	+0.16 ^{+1.10} _{–1.09}	...	+0.40 ^{+0.92} _{–0.90}
HD 128279	–0.02	–2.46	–0.06 ^{+1.14} _{–1.14}	...	+0.69 ^{+1.30} _{–1.22}	...	+0.32 ^{+0.89} _{–0.86}
HD 110184	–0.03	–2.52	+0.66 ^{+1.27} _{–1.18}	...	+0.50 ^{+1.07} _{–1.02}	...	+0.60 ^{+0.86} _{–0.80}
CS 22873-055	–0.19	–2.99	–1.25 ^{+1.01} _{–1.14}	...	–1.25 ^{+1.01} _{–1.14}
BD –18°5550	–0.22	–3.06	–2.04 ^{+1.04} _{–1.20}	...	–2.04 ^{+1.04} _{–1.20}
CS 22873-166	–0.32	–2.97	+1.18 ^{+1.34} _{–1.12}	...	–0.00 ^{+1.07} _{–1.04}	...	+0.62 ^{+0.87} _{–0.80}
HD 88609	–0.33	–3.07	–0.06 ^{+0.86} _{–0.83}	...	+0.06 ^{+0.78} _{–0.75}	+0.03 ^{+0.74} _{–0.70}	+0.02 ^{+0.48} _{–0.46}
HD 122563	–0.52	–2.77	–0.64 ^{+0.88} _{–0.90}	...	–0.27 ^{+0.81} _{–0.80}	–0.82 ^{+0.75} _{–0.77}	–0.58 ^{+0.49} _{–0.50}

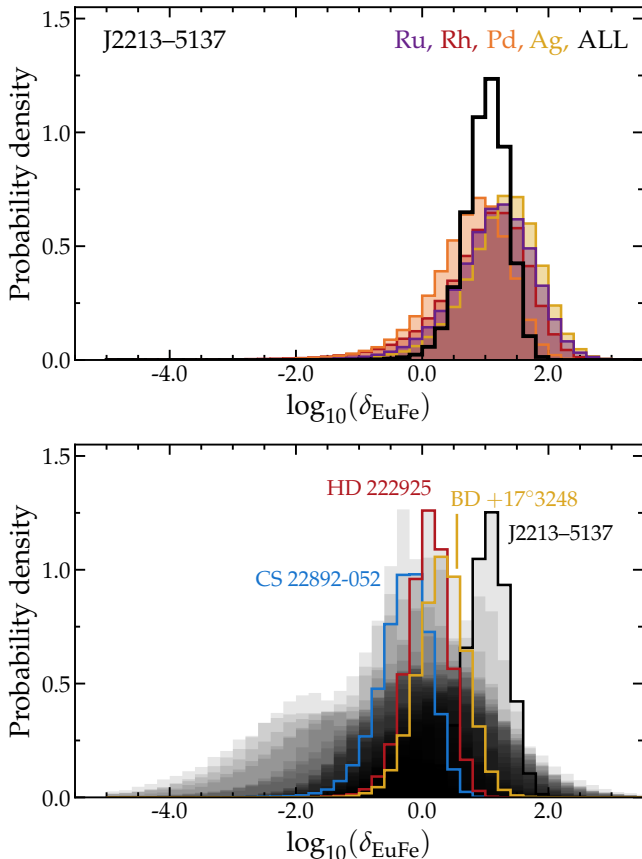


Figure 9. Probability distribution densities for δ_{EuFe} predicted using Equation 1 for the individual element ratios $\log \varepsilon(X/\text{Zr})$ in J2213–5137 (top panel) and probabilities combined from up to four individual element ratios found in 41 stars in the Roederer et al. (2023) sample (bottom panel). There are 42 stars in the Roederer et al. sample, but no abundances of Ru, Rh, Pd, or Ag have been reported for one of them, HD 140283. The distribution for each star is shown by a light gray region. By construction, they are centered around $\log \delta_{\text{EuFe}} = 0.0$. A few stars of note are labeled.

a few stars of note (Section 5.1) are labeled in Figure 9. J2213–5137 marks the low-dilution or high-yield extreme of the sample. We conclude that the r -process material from which J2213–5137 formed was mixed into an ISM that was ≈ 11 times (i.e., $10^{+1.04}$) less abundant in Fe than the typical star in the sample, or that the r -process event that enriched J2213–5137 ejected ≈ 11 times more r -process material than the typical event, or some combination of these two scenarios.

5.6. Exploring a Potential Dwarf Galaxy Connection

We investigate three potential connections between J2213–5137 and stars born in dwarf galaxies.

First, the age estimate for J2213–5137 calculated in Section 5.3, 13.6 ± 2.6 Gyr, matches the epoch of star formation in low-mass dwarf galaxies (Brown et al. 2014;

Weisz et al. 2014; Sacchi et al. 2021) and the oldest globular clusters (VandenBerg et al. 2013; Ying et al. 2023). A few stars that were likely formed in globular clusters are known in the halo (e.g., Ramírez et al. 2012; Lind et al. 2015; Martell et al. 2016), but we do not consider J2213–5137 to be one of them. J2213–5137 does not exhibit any of the abundance variations among light elements—such as O, Na, Mg, or Al—found in many stars in globular clusters (e.g., Carretta et al. 2009). It is therefore unlikely to have been formed as a member of the second, or chemically polluted, generation of stars formed within a globular cluster. Furthermore, the level of r -process enhancement is far in excess of any known stars within globular clusters (e.g., Gratton et al. 2004; Cabrera Garcia et al. 2024). In contrast, as noted in Section 1, stars in dwarf galaxies exhibit abundance patterns similar to that found in J2213–5137. This line of reasoning does not require a dwarf galaxy origin, but it is compatible with one.

Secondly, J2213–5137 is bound to the inner region of the Milky Way. It has an eccentric orbit ($e = 0.73$) with a small orbital pericenter ($r_{\text{peri}} = 1.1$ kpc). It is currently ($R = 7.0$ kpc) near its orbital apocenter ($r_{\text{apo}} = 7.2$ kpc), which is within the Sun’s orbital radius. These orbital characteristics are broadly similar to other r -II stars in the Solar neighborhood (Roederer et al. 2018a; Gudin et al. 2021; Hattori et al. 2023), but the orbit of J2213–5137 is distinct from them. For example, the orbit of the other r -III field star, J1521–3538, is much wider: $r_{\text{peri}} \approx 6$ kpc and $r_{\text{apo}} \approx 26$ kpc (Cain et al. 2020; Hattori et al. 2023). The orbit, actions, and energy of J2213–5137 differ from all stars in the Hattori et al. sample with $[\text{Eu}/\text{Fe}] > +1.7$. We conclude that it is unlikely that J2213–5137 formed alongside any of these stars.

The orbital properties of J2213–5137 overlap with the H22:DTC-15 chemodynamically tagged group of r -process-enhanced stars, which was identified by Hattori et al. (2023). The 18 members of this group have orbital pericenters < 1.2 kpc (mostly < 0.6 kpc), orbital apocenters of 6–12 kpc (mostly > 8 kpc), and radial but slightly prograde orbits. These stars exhibit a mean metallicity of -2.43 and a metallicity dispersion of 0.50 dex, and they include two of the comparison stars considered in Section 5.1, BD +17°3248 and CS 22892-052. Figure 6 compares the heavy-element abundance patterns of J2213–5137 and these two stars. Most of their abundance ratios are indistinguishable. As noted previously, however, the $\log \varepsilon(\text{Ru,Rh,Pd,Ag}/\text{Zr})$ ratios are higher in CS 22892-052 than in J2213–5137 by about 0.1 dex, and these same ratios are lower in BD +17°3248 by about 0.2 dex. This difference implies that the r -process material found in these three stars could not have originated in only one r -process event. Two or more r -process events could have enriched the putative progenitor dwarf galaxy, which is unlikely because of the low occurrence frequency of r -process-

enhanced dwarf galaxies today (Ji et al. 2016a). Alternatively, H22:DTC-15 could include stars from several accretion events, and therefore J2213–5137 may not actually share an origin with either of these stars. This association should be reassessed once larger samples of r -process-enhanced stars have been identified.

Thirdly, the [Fe/H] and [Eu/Fe] ratios of J2213–5137 are suggestive of a dwarf galaxy environment. If J2213–5137 formed in an environment where an average r -process event’s yield was diluted into an average amount of Fe, it would exhibit [Fe/H] = $-2.20 + 1.04 = -1.16$ and [Eu/Fe] = $+2.45 - 1.04 = +1.41$. (We derived the value 1.04 in Section 5.5.) While these ratios are rare among field stars, they are found among several r -process-enhanced stars in the Fornax dwarf galaxy (Reichert et al. 2021).

We explore this potential connection further by expressing the relationship between the H, Fe, and Eu abundances using standard abundance definitions and the Solar abundance ratios:

$$M_{\text{H}} = M_{\text{Eu}} \cdot 10^{9.30 - [\text{Eu}/\text{H}]}, \text{ or} \quad (2)$$

$$M_{\text{Eu}} = M_{\text{H}} \cdot 10^{[\text{Eu}/\text{H}] - 9.30}. \quad (3)$$

Note that the mass of Eu ejected by an r -process event (M_{Eu}) equals $\approx 10^{-3}$ times the mass of r -process elements (M_r) in a standard r -process abundance pattern, such as that found in the Solar System. If the [Eu/H] ratio is known, and either of the dilution mass of H (M_{H}) or M_{Eu} can be estimated, the third quantity can be calculated. A comparison sample of six other stars with [Eu/Fe] > +1.3 listed in Table 5 exhibits a mean [Eu/H] of -0.97 ± 0.26 . For a canonical baryonic minihalo mass of $M_{\text{H}} = 10^6 M_{\odot}$ (e.g., Tegmark et al. 1997), Equation 3 predicts an average yield of $M_{\text{Eu}} \approx 5 \times 10^{-5} M_{\odot}$, or $M_r \approx 5 \times 10^{-2} M_{\odot}$, for the r -process nucleosynthesis events that enriched the comparison sample.

Using this r -process yield, Equation 2 predicts J2213–5137 would have formed from gas with $M_{\text{H}} \approx 6 \times 10^4 M_{\odot}$, assuming that the r -process material is well mixed into the gas. This mass would be even lower if most of the r -process material was lost to the intergalactic medium, rather than incorporated into stars. Beniamini et al. (2018) estimated that a large fraction, 90%, of r -process material could be retained in dwarf galaxies that had not already lost a large fraction of their gas. The retainment fraction might also be a strong function of where r -process material is injected into a dwarf galaxy (Safarzadeh & Scannapieco 2017; Tarumi et al. 2020), the timing of the r -process enrichment (Bonetti et al. 2019), and the mass of the galaxy itself (Cavallo et al. 2023). If only $\sim 1\%$ of r -process material was retained in stars, as inferred from lighter metals in dwarf galaxies (e.g., Kirby et al. 2011; McQuinn et al. 2015; Emerick et al. 2018), then the r -process material retained would have been diluted into only $\sim 600 M_{\odot}$ of gas. This gas cloud would have already been enriched

by light elements produced in normal ratios by typical core-collapse supernovae. In this scenario, very few stars with [Eu/Fe] ratios as high as that found in J2213–5137 could have formed.

6. SUMMARY AND CONCLUSIONS

J2213–5137 was observed using the MIKE spectrograph at Magellan as part of the high-resolution spectroscopic followup of metal-poor star candidates conducted by the RPA. We immediately recognized the strong lines of lanthanides and other heavy elements in its spectrum (Figures 1–4). We derive stellar parameters (Table 1) that place this metal-poor star ([Fe/H] = -2.20) on the red horizontal branch ($T_{\text{eff}} = 5509$ K, $\log g = 2.28$). We calculate the kinematics of J2213–5137, and we find that it follows an eccentric orbit confined within the Solar circle ($r_{\text{peri}} = 1.1$ kpc, $r_{\text{apo}} = 7.2$ kpc). We derive abundances of 47 metals detected in its optical spectrum, and we derive upper limits on six other elements based on non-detections (Table 3). The abundances of light elements ($Z \leq 30$) in J2213–5137 are typical for metal-poor halo stars. The abundances of heavier elements, in contrast, are highly enhanced (e.g., [Eu/Fe] = +2.45), including many with super-Solar [X/H] ratios (e.g., [Eu/H] = +0.25), and it is a member of the class of r -III stars that was proposed by Cain et al. (2020). The heavy-element abundance pattern is a close match to the r -process abundance pattern inferred for the Sun (Figure 5) and well-studied r -process-enhanced stars (Figure 6). We detect radioactive isotopes of thorium and uranium, and we calculate an age of 13.6 ± 2.6 Gyr for the r -process material in J2213–5137 (Figure 7, Table 4).

We investigate what may have led to the high level of r -process enhancement in J2213–5137. We propose a new method to assess the relative dilution or relative yields of r -process material incorporated into a star (Section 5.5). This method makes use of the correlation between the $\log \varepsilon(\text{Ru,Rh,Pd,Ag/Zr})$ ratios and the [Eu/Fe] ratio in metal-poor r -process-enhanced stars (Roederer et al. 2023). J2213–5137 exhibits $\log \varepsilon(\text{Ru,Rh,Pd,Ag/Zr})$ ratios that are similar to other stars with [Eu/Fe] > +1.3, suggesting that the yields of the r -process events that enriched these stars may have been similar. We conclude that J2213–5137 exhibits a high level of r -process enhancement because it formed in an environment where the r -process material was less diluted than average. If we assume a canonical baryonic minihalo mass of $10^6 M_{\odot}$ and 1% retention of r -process material in star-forming gas, then J2213–5137 would have formed where $\approx 0.05 M_{\odot}$ of r -process material was diluted into $\approx 600 M_{\odot}$ of gas. This order-of-magnitude estimate requires several simplifying assumptions, as discussed in Sections 5.5 and 5.6, but it may suggest why stars like J2213–5137 are relatively uncommon.

ACKNOWLEDGMENTS

In memory of Jim Lawler (1951–2023), an uncommonly meticulous scientist and patient mentor.

We thank John Cowan for helpful feedback on an earlier version of the manuscript, and we thank the anonymous referee for thoughtful suggestions that have improved the manuscript. We acknowledge support from the U.S. National Science Foundation (NSF): grants PHY 14-30152 (Physics Frontier Center/JINA-CEE), OISE 1927130 (International Research Network for Nuclear Astrophysics/IRENA), AST 1716251 (A.F.), AST 1815403/1815767 and AST 2205847 (I.U.R.), and AST-2206263 (R.E.). I.U.R. acknowledges support from the NASA Astrophysics Data Analysis Program, grant 80NSSC21K0627. K.H. is supported by JSPS KAKENHI Grant Numbers JP21K13965 and JP21H00053. The work of V.M.P. is supported by NOIRLab, which is managed by AURA under a cooperative agreement with the NSF. This research has made

use of NASA’s Astrophysics Data System Bibliographic Services; the arXiv preprint server operated by Cornell University; the SIMBAD and VizieR databases hosted by the Strasbourg Astronomical Data Center; the ASD hosted by NIST; and the IRAF software packages distributed by the National Optical Astronomy Observatories, which are operated by AURA, under cooperative agreement with the NSF. This work has also made use of data from the European Space Agency (ESA) mission Gaia (<https://www.cosmos.esa.int/gaia>), processed by the Gaia DPAC (<https://www.cosmos.esa.int/web/gaia/dpac/consortium>). Funding for the DPAC has been provided by national institutions, in particular the institutions participating in the Gaia Multilateral Agreement.

Facility: Magellan II (MIKE)

Software: AGAMA (Vasiliev 2019), IRAF (Tody 1993), LINEMAKE (Placco et al. 2021), Matplotlib (Hunter 2007), MOOG (Snedden 1973; Sobeck et al. 2011), NumPy (van der Walt et al. 2011), R (R Core Team 2013), SciPy (Jones et al. 2001)

APPENDIX

A. AGES CALCULATED FROM RADIOGENIC LEAD PRODUCTION

Following Clayton (1964), the abundance of each Pb isotope at time t , where t is expressed in Gyr, is given by

$$\begin{aligned} {}^{206}\text{Pb}(t) &= {}^{206}\text{Pb}_r + {}^{206}\text{Pb}_c + {}^{206}\text{Pb}_s \\ {}^{207}\text{Pb}(t) &= {}^{207}\text{Pb}_r + {}^{207}\text{Pb}_c + {}^{207}\text{Pb}_s \\ {}^{208}\text{Pb}(t) &= {}^{208}\text{Pb}_r + {}^{208}\text{Pb}_c + {}^{208}\text{Pb}_s, \end{aligned} \quad (\text{A1})$$

where

$$\begin{aligned} {}^{206}\text{Pb}_c &= {}^{238}\text{U}_r - {}^{238}\text{U}_r(t) \\ {}^{207}\text{Pb}_c &= {}^{235}\text{U}_r - {}^{235}\text{U}_r(t) \\ {}^{208}\text{Pb}_c &= {}^{232}\text{Th}_r - {}^{232}\text{Th}_r(t) \end{aligned} \quad (\text{A2})$$

and

$$\begin{aligned} {}^{238}\text{U}_r(t) &= {}^{238}\text{U}_r - {}^{238}\text{U}_r(1 - e^{-t \ln 2/4.468}) \\ {}^{235}\text{U}_r(t) &= {}^{235}\text{U}_r - {}^{235}\text{U}_r(1 - e^{-t \ln 2/0.7038}) \\ {}^{232}\text{Th}_r(t) &= {}^{232}\text{Th}_r - {}^{232}\text{Th}_r(1 - e^{-t \ln 2/14.0}). \end{aligned} \quad (\text{A3})$$

In these equations, the subscript r denotes the direct isobaric r -process contribution and the contribution from short-lived translead or transuranic isotopes; c denotes the cosmoradiogenic decay of the long-lived ${}^{232}\text{Th}$, ${}^{235}\text{U}$, and ${}^{238}\text{U}$ isotopes in the time interval between nucleosynthesis and the present day; and s denotes the s -process contribution. The values of ${}^A X_r$ are calculated theoretically (e.g., Kratz et al. 2007; Roederer et al. 2009). The total Pb abundance is thus

$$\text{Pb} = {}^{204}\text{Pb} + {}^{206}\text{Pb} + {}^{207}\text{Pb} + {}^{208}\text{Pb}. \quad (\text{A4})$$

The ${}^{204}\text{Pb}$ isotope is blocked from r -process production by ${}^{204}\text{Hg}$. We assume that the s -process contribution to the Pb abundance in J2213–5137 is zero. The Pb abundance at time t is given by

$$\text{Pb}(t) = {}^{206}\text{Pb}_r + {}^{207}\text{Pb}_r + {}^{208}\text{Pb}_r + {}^{238}\text{U}_r(1 - e^{-t \ln 2/4.468}) + {}^{235}\text{U}_r(1 - e^{-t \ln 2/0.7038}) + {}^{232}\text{Th}_r(1 - e^{-t \ln 2/14.0}) \quad (\text{A5})$$

Equation A5 is not easily solved analytically for t , so we resort to numerical methods to estimate t from the observed ratios among the Pb, Th, and U abundances in Section 5.2.

REFERENCES

- Alonso, A., Arribas, S., & Martínez-Roger, C. 1999, *A&AS*, 140, 261
- Amarsi, A. M., Asplund, M., Collet, R., & Leenaarts, J. 2015, *MNRAS*, 454, L11
- Aoki, W., Beers, T. C., Honda, S., & Carollo, D. 2010, *ApJL*, 723, L201
- Asplund, M., Grevesse, N., Sauval, A. J., & Scott, P. 2009, *ARA&A*, 47, 481
- Bailer-Jones, C. A. L., Rybizki, J., Fouesneau, M., Demleitner, M., & Andrae, R. 2021, *AJ*, 161, 147
- Battistini, C., & Bensby, T. 2016, *A&A*, 586, A49
- Belmonte, M. T., Pickering, J. C., Ruffoni, M. P., et al. 2017, *ApJ*, 848, 125
- Beniamini, P., Dvorkin, I., & Silk, J. 2018, *MNRAS*, 478, 1994
- Beniamini, P., Hotokezaka, K., & Piran, T. 2016, *ApJ*, 832, 149
- Bergemann, M. 2011, *MNRAS*, 413, 2184
- Bergemann, M., Lind, K., Collet, R., Magic, Z., & Asplund, M. 2012, *MNRAS*, 427, 27
- Bernstein, R., Shtetman, S. A., Gunnels, S. M., Mochnacki, S., & Athey, A. E. 2003, in *Proc. SPIE*, Vol. 4841, *Instrument Design and Performance for Optical/Infrared Ground-based Telescopes*, ed. M. Iye & A. F. M. Moorwood, 1694–1704
- Bianchi, L., Shiao, B., & Thilker, D. 2017, *ApJS*, 230, 24
- Biémont, E., Garnir, H. P., Palmeri, P., Li, Z. S., & Svanberg, S. 2000, *MNRAS*, 312, 116
- Biemont, E., Grevesse, N., Kwiatkowski, M., & Zimmermann, P. 1982, *A&A*, 108, 127
- Biémont, É., Blagoev, K., Engström, L., et al. 2011, *MNRAS*, 414, 3350
- Bisterzo, S., Travaglio, C., Gallino, R., Wiescher, M., & Käppeler, F. 2014, *ApJ*, 787, 10
- Bonetti, M., Perego, A., Dotti, M., & Cescutti, G. 2019, *MNRAS*, 490, 296
- Brown, T. M., Tumlinson, J., Geha, M., et al. 2014, *ApJ*, 796, 91
- Cabrera Garcia, J., Sakari, C. M., Roederer, I. U., et al. 2024, *The Astrophysical Journal*, 967, 101
- Cain, M., Frebel, A., Ji, A. P., et al. 2020, *ApJ*, 898, 40
- Carretta, E., Bragaglia, A., Gratton, R., & Lucatello, S. 2009, *A&A*, 505, 139
- Casagrande, L., Ramírez, I., Meléndez, J., Bessell, M., & Asplund, M. 2010, *A&A*, 512, A54
- Casagrande, L., & Vandenberg, D. A. 2014, *MNRAS*, 444, 392
- Castelli, F., & Kurucz, R. L. 2004, *ArXiv e-prints*. <https://arxiv.org/abs/astro-ph/0405087>
- Cavallo, L., Cescutti, G., & Matteucci, F. 2023, *A&A*, 674, A130
- Cayrel, R., Hill, V., Beers, T. C., et al. 2001, *Nature*, 409, 691
- Clayton, D. D. 1964, *ApJ*, 139, 637
- Cowan, J. J., McWilliam, A., Sneden, C., & Burris, D. L. 1997, *ApJ*, 480, 246
- Cowan, J. J., Pfeiffer, B., Kratz, K.-L., et al. 1999, *ApJ*, 521, 194
- Cowan, J. J., Sneden, C., Lawler, J. E., et al. 2021, *Reviews of Modern Physics*, 93, 015002
- Cowan, J. J., Thielemann, F. K., & Truran, J. W. 1987, *ApJ*, 323, 543
- Cowan, J. J., Sneden, C., Burles, S., et al. 2002, *ApJ*, 572, 861
- Cowan, J. J., Sneden, C., Beers, T. C., et al. 2005, *ApJ*, 627, 238
- Cutri, R. M., Skrutskie, M. F., van Dyk, S., et al. 2003, *VizieR Online Data Catalog*, 2246
- Delgado Mena, E., Tsantaki, M., Adibekyan, V. Z., et al. 2017, *A&A*, 606, A94
- Den Hartog, E. A., Herd, M. T., Lawler, J. E., et al. 2005, *ApJ*, 619, 639
- Den Hartog, E. A., Lawler, J. E., Sneden, C., & Cowan, J. J. 2003, *ApJS*, 148, 543
- . 2006, *ApJS*, 167, 292
- Den Hartog, E. A., Lawler, J. E., Sneden, C., Cowan, J. J., & Brukhovesky, A. 2019, *ApJS*, 243, 33
- Den Hartog, E. A., Lawler, J. E., Sneden, C., et al. 2021, *ApJS*, 255, 27
- Den Hartog, E. A., Lawler, J. E., Sobeck, J. S., Sneden, C., & Cowan, J. J. 2011, *ApJS*, 194, 35
- Den Hartog, E. A., Ruffoni, M. P., Lawler, J. E., et al. 2014, *ApJS*, 215, 23
- Duquette, D. W., & Lawler, J. E. 1985, *Journal of the Optical Society of America B Optical Physics*, 2, 1948
- Emerick, A., Bryan, G. L., Mac Low, M.-M., et al. 2018, *ApJ*, 869, 94
- Ezzeddine, R., Frebel, A., & Plez, B. 2017, *ApJ*, 847, 142
- Ezzeddine, R., Rasmussen, K., Frebel, A., et al. 2020, *ApJ*, 898, 150

- Fowler, W. A., & Hoyle, F. 1960, *Annals of Physics*, 10, 280
- Frebel, A., Christlieb, N., Norris, J. E., et al. 2007, *ApJL*, 660, L117
- Gaia Collaboration, Prusti, T., de Bruijne, J. H. J., et al. 2016, *A&A*, 595, A1
- Gaia Collaboration, Babusiaux, C., van Leeuwen, F., et al. 2018, *A&A*, 616, A10
- Gaia Collaboration, Vallenari, A., Brown, A. G. A., et al. 2022, arXiv e-prints, arXiv:2208.00211
- Gratton, R., Sneden, C., & Carretta, E. 2004, *ARA&A*, 42, 385
- Gratton, R. G., Sneden, C., Carretta, E., & Bragaglia, A. 2000, *A&A*, 354, 169
- GRAVITY Collaboration, Abuter, R., Amorim, A., et al. 2019, *A&A*, 625, L10
- Gudin, D., Shank, D., Beers, T. C., et al. 2021, *ApJ*, 908, 79
- Guiglion, G., de Laverny, P., Recio-Blanco, A., & Prantzos, N. 2018, *A&A*, 619, A143
- Hansen, C. J., Primas, F., Hartman, H., et al. 2012, *A&A*, 545, A31
- Hansen, T. T., Holmbeck, E. M., Beers, T. C., et al. 2018, *ApJ*, 858, 92
- Hansen, T. T., Ji, A. P., Da Costa, G. S., et al. 2021, *ApJ*, 915, 103
- Hattori, K., Okuno, A., & Roederer, I. U. 2023, *ApJ*, 946, 48
- Hayes, C. R., Venn, K. A., Waller, F., et al. 2023, *ApJ*, 955, 17
- Hill, V., Christlieb, N., Beers, T. C., et al. 2017, *A&A*, 607, A91
- Hill, V., Plez, B., Cayrel, R., et al. 2002, *A&A*, 387, 560
- Hirai, Y., Beers, T. C., Chiba, M., et al. 2022, *MNRAS*, 517, 4856
- Holmbeck, E. M., Sprouse, T. M., Mumpower, M. R., et al. 2019, *ApJ*, 870, 23
- Holmbeck, E. M., Beers, T. C., Roederer, I. U., et al. 2018, *ApJL*, 859, L24
- Holmbeck, E. M., Hansen, T. T., Beers, T. C., et al. 2020, *ApJS*, 249, 30
- Honda, S., Aoki, W., Kajino, T., et al. 2004, *ApJ*, 607, 474
- Hunter, J. D. 2007, *Computing in Science and Engineering*, 9, 90
- Ivans, I. I., Simmerer, J., Sneden, C., et al. 2006, *ApJ*, 645, 613
- Ivarsson, S., Litzén, U., & Wahlgren, G. M. 2001, *PhyS*, 64, 455
- Jacobson, H. R., Keller, S., Frebel, A., et al. 2015, *ApJ*, 807, 171
- Ji, A. P., Frebel, A., Chiti, A., & Simon, J. D. 2016a, *Nature*, 531, 610
- Ji, A. P., Frebel, A., Simon, J. D., & Chiti, A. 2016b, *ApJ*, 830, 93
- Ji, A. P., Li, T. S., Simon, J. D., et al. 2020, *ApJ*, 889, 27
- Ji, A. P., Simon, J. D., Roederer, I. U., et al. 2023, *AJ*, 165, 100
- Johnson, J. A., & Bolte, M. 2001, *ApJ*, 554, 888
- Jones, E., Oliphant, T., Peterson, P., & et al. 2001, *SciPy: Open source scientific tools for Python*, online. <http://www.scipy.org/>
- Katz, D., Sartoretti, P., Guerrier, A., et al. 2022, arXiv e-prints, arXiv:2206.05902
- Kelson, D. D. 2003, *PASP*, 115, 688
- Kelson, D. D., Illingworth, G. D., van Dokkum, P. G., & Franx, M. 2000, *ApJ*, 531, 159
- Kirby, E. N., Martin, C. L., & Finlator, K. 2011, *ApJL*, 742, L25
- Kordopatis, G., Gilmore, G., Steinmetz, M., et al. 2013, *AJ*, 146, 134
- Kramida, A., Ralchenko, Y., Reader, J., & NIST ASD Team. 2021, *NIST Atomic Spectra Database (ver. 5.9)*, [Online]. Available: <https://physics.nist.gov/asd>, National Institute of Standards and Technology, Gaithersburg, MD.
- Kratz, K.-L., Farouqi, K., Pfeiffer, B., et al. 2007, *ApJ*, 662, 39
- Kunder, A., Kordopatis, G., Steinmetz, M., et al. 2017, *AJ*, 153, 75
- Kurucz, R. L. 2011, *Canadian Journal of Physics*, 89, 417
- Lawler, J. E., Bonvallet, G., & Sneden, C. 2001a, *ApJ*, 556, 452
- Lawler, J. E., & Dakin, J. T. 1989, *Journal of the Optical Society of America B Optical Physics*, 6, 1457
- Lawler, J. E., den Hartog, E. A., Labby, Z. E., et al. 2007, *ApJS*, 169, 120
- Lawler, J. E., Den Hartog, E. A., Sneden, C., & Cowan, J. J. 2006, *ApJS*, 162, 227
- Lawler, J. E., Guzman, A., Wood, M. P., Sneden, C., & Cowan, J. J. 2013, *ApJS*, 205, 11
- Lawler, J. E., Sneden, C., & Cowan, J. J. 2004, *ApJ*, 604, 850
- . 2015, *ApJS*, 220, 13
- Lawler, J. E., Sneden, C., Cowan, J. J., Ivans, I. I., & Den Hartog, E. A. 2009, *ApJS*, 182, 51
- Lawler, J. E., Sneden, C., Cowan, J. J., et al. 2008, *ApJS*, 178, 71
- Lawler, J. E., Sneden, C., Nave, G., et al. 2017, *ApJS*, 228, 10
- Lawler, J. E., Wickliffe, M. E., Cowley, C. R., & Sneden, C. 2001b, *ApJS*, 137, 341

- Lawler, J. E., Wickliffe, M. E., den Hartog, E. A., & Sneden, C. 2001c, *ApJ*, 563, 1075
- Lawler, J. E., Wood, M. P., Den Hartog, E. A., et al. 2014, *ApJS*, 215, 20
- Lawler, J. E., Wyart, J.-F., & Blaise, J. 2001d, *ApJS*, 137, 351
- Li, H., Aoki, W., Matsuno, T., et al. 2022, *ApJ*, 931, 147
- Li, R., Chatelain, R., Holt, R. A., et al. 2007, *PhyS*, 76, 577
- Li, Z. S., Norin, J., Persson, A., et al. 1999, *PhRvA*, 60, 198
- Lind, K., Asplund, M., Barklem, P. S., & Belyaev, A. K. 2011, *A&A*, 528, A103
- Lind, K., Bergemann, M., & Asplund, M. 2012, *MNRAS*, 427, 50
- Lind, K., Melendez, J., Asplund, M., Collet, R., & Magic, Z. 2013, *A&A*, 554, A96
- Lind, K., Koposov, S. E., Battistini, C., et al. 2015, *A&A*, 575, L12
- Lindgren, L., Klioner, S. A., Hernández, J., et al. 2021, *A&A*, 649, A2
- Ljung, G., Nilsson, H., Asplund, M., & Johansson, S. 2006, *A&A*, 456, 1181
- Lodders, K. 2003, *ApJ*, 591, 1220
- Magg, E., Bergemann, M., Serenelli, A., et al. 2022, *A&A*, 661, A140
- Martell, S. L., Shetrone, M. D., Lucatello, S., et al. 2016, *ApJ*, 825, 146
- Mashonkina, L., Christlieb, N., & Eriksson, K. 2014, *A&A*, 569, A43
- Mashonkina, L., Ryabtsev, A., & Frebel, A. 2012, *A&A*, 540, A98
- Mathews, G. J., & Schramm, D. N. 1988, *ApJL*, 324, L67
- McMillan, P. J. 2017, *MNRAS*, 465, 76
- McQuinn, K. B. W., Skillman, E. D., Dolphin, A., et al. 2015, *ApJL*, 815, L17
- McWilliam, A. 1998, *AJ*, 115, 1640
- Meija, J., Coplen, M. B., Berglund, M., et al. 2016, *Pure and Applied Chemistry*, 88, 293
- Meléndez, J., & Barbuy, B. 2009, *A&A*, 497, 611
- Molero, M., Romano, D., Reichert, M., et al. 2021, *MNRAS*, 505, 2913
- Morton, D. C. 2000, *ApJS*, 130, 403
- Mucciarelli, A., Bellazzini, M., & Massari, D. 2021, *A&A*, 653, A90
- Munari, U., Henden, A., Frigo, A., et al. 2014, *AJ*, 148, 81
- Nilsson, H., Ivarsson, S., Johansson, S., & Lundberg, H. 2002a, *A&A*, 381, 1090
- Nilsson, H., Zhang, Z. G., Lundberg, H., Johansson, S., & Nordström, B. 2002b, *A&A*, 382, 368
- Nilsson, H., Hartman, H., Engström, L., et al. 2010, *A&A*, 511, A16
- Nordlander, T., & Lind, K. 2017, *A&A*, 607, A75
- O'Brian, T. R., Wickliffe, M. E., Lawler, J. E., Whaling, W., & Brault, J. W. 1991, *Journal of the Optical Society of America B Optical Physics*, 8, 1185
- Ojima, T., Ishimaru, Y., Wanajo, S., Prantzos, N., & François, P. 2018, *ApJ*, 865, 87
- Pakhomov, Y. V., Ryabchikova, T. A., & Piskunov, N. E. 2019, *Astronomy Reports*, 63, 1010
- Pehlivan Rhodin, A., Hartman, H., Nilsson, H., & Jönsson, P. 2017, *A&A*, 598, A102
- Piskunov, N. E., Kupka, F., Ryabchikova, T. A., Weiss, W. W., & Jeffery, C. S. 1995, *A&AS*, 112, 525
- Placco, V. M., Frebel, A., Beers, T. C., & Stancliffe, R. J. 2014, *ApJ*, 797, 21
- Placco, V. M., Sneden, C., Roederer, I. U., et al. 2021, *Research Notes of the American Astronomical Society*, 5, 92
- Placco, V. M., Holmbeck, E. M., Frebel, A., et al. 2017, *ApJ*, 844, 18
- Placco, V. M., Beers, T. C., Santucci, R. M., et al. 2018, *AJ*, 155, 256
- Quinet, P., Palmeri, P., Biémont, É., et al. 2006, *A&A*, 448, 1207
- R Core Team. 2013, *R: A Language and Environment for Statistical Computing*, R Foundation for Statistical Computing, Vienna, Austria.
<http://www.R-project.org/>
- Ramírez, I., & Meléndez, J. 2005, *ApJ*, 626, 465
- Ramírez, I., Meléndez, J., & Chanamé, J. 2012, *ApJ*, 757, 164
- Reichert, M., Hansen, C. J., & Arcones, A. 2021, *ApJ*, 912, 157
- Reid, M. J., & Brunthaler, A. 2004, *ApJ*, 616, 872
- Ren, J., Christlieb, N., & Zhao, G. 2012, *A&A*, 537, A118
- Riello, M., De Angeli, F., Evans, D. W., et al. 2021, *A&A*, 649, A3
- Roederer, I. U., & Barklem, P. S. 2018, *ApJ*, 857, 2
- Roederer, I. U., Hattori, K., & Valluri, M. 2018a, *AJ*, 156, 179
- Roederer, I. U., Kratz, K.-L., Frebel, A., et al. 2009, *ApJ*, 698, 1963
- Roederer, I. U., & Lawler, J. E. 2012, *ApJ*, 750, 76
- . 2021, *ApJ*, 912, 119
- Roederer, I. U., Lawler, J. E., Sneden, C., et al. 2008, *ApJ*, 675, 723
- Roederer, I. U., Preston, G. W., Thompson, I. B., et al. 2014, *AJ*, 147, 136
- Roederer, I. U., Sakari, C. M., Placco, V. M., et al. 2018b, *ApJ*, 865, 129

- Roederer, I. U., Sneden, C., Lawler, J. E., et al. 2018c, *ApJ*, 860, 125
- Roederer, I. U., Lawler, J. E., Sobeck, J. S., et al. 2012, *ApJS*, 203, 27
- Roederer, I. U., Mateo, M., Bailey, III, J. I., et al. 2016, *AJ*, 151, 82
- Roederer, I. U., Lawler, J. E., Holmbeck, E. M., et al. 2020, *ApJL*, 902, L24
- Roederer, I. U., Lawler, J. E., Den Hartog, E. A., et al. 2022a, *ApJS*, 260, 27
- Roederer, I. U., Cowan, J. J., Pignatari, M., et al. 2022b, *ApJ*, 936, 84
- Roederer, I. U., Vassh, N., Holmbeck, E. M., et al. 2023, *Science*, 382, 1177
- Ruffoni, M. P., Den Hartog, E. A., Lawler, J. E., et al. 2014, *MNRAS*, 441, 3127
- Sacchi, E., Richstein, H., Kallivayalil, N., et al. 2021, *ApJL*, 920, L19
- Safarzadeh, M., & Scannapieco, E. 2017, *MNRAS*, 471, 2088
- Sakari, C. M., Placco, V. M., Farrell, E. M., et al. 2018, *ApJ*, 868, 110
- Saraf, P., Allende Prieto, C., Sivarani, T., et al. 2023, *MNRAS*, 524, 5607
- Schatz, H., Toenjes, R., Pfeiffer, B., et al. 2002, *ApJ*, 579, 626
- Schlafly, E. F., & Finkbeiner, D. P. 2011, *ApJ*, 737, 103
- Shah, S. P., Ezzeddine, R., Ji, A. P., et al. 2023, *ApJ*, 948, 122
- Shank, D., Beers, T. C., Placco, V. M., et al. 2023, *ApJ*, 943, 23
- Shi, J. R., Yan, H. L., Zhou, Z. M., & Zhao, G. 2018, *ApJ*, 862, 71
- Simmerer, J., Sneden, C., Cowan, J. J., et al. 2004, *ApJ*, 617, 1091
- Siqueira Mello, C., Spite, M., Barbuy, B., et al. 2013, *A&A*, 550, A122
- Smith, V. V., Lambert, D. L., & Nissen, P. E. 1998, *ApJ*, 506, 405
- Sneden, C., Cowan, J. J., & Gallino, R. 2008, *ARA&A*, 46, 241
- Sneden, C., Lawler, J. E., Cowan, J. J., Ivans, I. I., & Den Hartog, E. A. 2009, *ApJS*, 182, 80
- Sneden, C., Preston, G. W., McWilliam, A., & Searle, L. 1994, *ApJL*, 431, L27
- Sneden, C., Cowan, J. J., Lawler, J. E., et al. 2003, *ApJ*, 591, 936
- Sneden, C. A. 1973, PhD thesis, The University of Texas at Austin.
- Sobeck, J. S., Lawler, J. E., & Sneden, C. 2007, *ApJ*, 667, 1267
- Sobeck, J. S., Kraft, R. P., Sneden, C., et al. 2011, *AJ*, 141, 175
- Takeda, Y., Zhao, G., Chen, Y.-Q., Qiu, H.-M., & Takada-Hidai, M. 2002, *PASJ*, 54, 275
- Tarumi, Y., Yoshida, N., & Inoue, S. 2020, *MNRAS*, 494, 120
- Tegmark, M., Silk, J., Rees, M. J., et al. 1997, *ApJ*, 474, 1
- Thévenin, F., & Idiart, T. P. 1999, *ApJ*, 521, 753
- Thielemann, F. K., Metzinger, J., & Klapdor, H. V. 1983, *A&A*, 123, 162
- Tody, D. 1993, in *Astronomical Society of the Pacific Conference Series*, Vol. 52, *Astronomical Data Analysis Software and Systems II*, ed. R. J. Hanisch, R. J. V. Brissenden, & J. Barnes, 173
- van der Walt, S., Colbert, S. C., & Varoquaux, G. 2011, *Computing in Science Engineering*, 13, 22
- VandenBerg, D. A., Brogaard, K., Leaman, R., & Casagrande, L. 2013, *ApJ*, 775, 134
- Vasiliev, E. 2019, *MNRAS*, 482, 1525
- Weisz, D. R., Dolphin, A. E., Skillman, E. D., et al. 2014, *ApJ*, 789, 147
- Wickliffe, M. E., & Lawler, J. E. 1997, *Journal of the Optical Society of America B Optical Physics*, 14, 737
- Wickliffe, M. E., Lawler, J. E., & Nave, G. 2000, *JQSRT*, 66, 363
- Wickliffe, M. E., Salih, S., & Lawler, J. E. 1994, *JQSRT*, 51, 545
- Wood, M. P., Lawler, J. E., Den Hartog, E. A., Sneden, C., & Cowan, J. J. 2014a, *ApJS*, 214, 18
- Wood, M. P., Lawler, J. E., Sneden, C., & Cowan, J. J. 2013, *ApJS*, 208, 27
- . 2014b, *ApJS*, 211, 20
- Xu, H. L., Svanberg, S., Quinet, P., Palmeri, P., & Biémont, É. 2007, *JQSRT*, 104, 52
- Ying, J. M., Chaboyer, B., Boudreaux, E. M., et al. 2023, *AJ*, 166, 18
- Yong, D., Kobayashi, C., Da Costa, G. S., et al. 2021, *Nature*, 595, 223
- Yuan, Z., Myeong, G. C., Beers, T. C., et al. 2020, *ApJ*, 891, 39